

ESD ACCESSION LIST

Call No.

71889

Copy No.

1

of

2

cys.

3

Solid State Research

1970

Prepared under Electronic Systems Division Contract AF 19(628)-5167 by

Lincoln Laboratory

MASSACHUSETTS INSTITUTE OF TECHNOLOGY

Lexington, Massachusetts



A00714079

This document has been approved for public release and sale,  
its distribution is unlimited.

3

# Solid State Research

1970

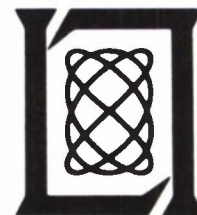
Issued 16 October 1970

Prepared under Electronic Systems Division Contract AF 19(628)-5167 by

## Lincoln Laboratory

MASSACHUSETTS INSTITUTE OF TECHNOLOGY

Lexington, Massachusetts



This document has been approved for public release and sale; its distribution is unlimited.

The work reported in this document was performed at Lincoln Laboratory, a center for research operated by Massachusetts Institute of Technology, with the support of the Department of the Air Force under Contract AF 19(628)-5167.

This report may be reproduced to satisfy needs of U.S. Government agencies.

Non-Lincoln Recipients

**PLEASE DO NOT RETURN**

Permission is given to destroy this document  
when it is no longer needed.



#### ABSTRACT

This report covers in detail the solid state research work of the Solid State Division at Lincoln Laboratory for the period 1 May through 31 July 1970. The topics covered are Solid State Device Research, Materials Research, Physics of Solids, and Microelectronics. The Microsound work is sponsored by ABMDA and is reported under that program.

Accepted for the Air Force  
Joseph R. Waterman, Lt. Col., USAF  
Chief, Lincoln Laboratory Project Office

# INTRODUCTION

## I. SOLID STATE DEVICE RESEARCH

Long-wavelength  $\text{Hg}_{0.821}\text{Cd}_{0.179}\text{Te}$  photovoltaic detectors have been fabricated by diffusion with peak detectivities near  $30\mu$  of about  $1 \times 10^{10} \text{ cm}\sqrt{\text{Hz}}/\text{W}$  at  $4.2^\circ\text{K}$ . Diodes fabricated from a smaller bandgap crystal showed photoresponse out to the  $48\text{-}\mu$  wavelength limit of the spectrometer used.

The  $\text{Hg}_{1-x}\text{Cd}_x\text{Te}$  crystals were grown by a new technique in which the vertical ampoule remains stationary in a temperature gradient at the melting point, and growth occurs via a near steady-state mass transfer in the liquid phase. High-quality single crystals produced by this technique were homogeneous in cross section with respect to Cd-Hg ratio with a small longitudinal gradient. Temperature gradient annealing has resulted in electron carrier concentrations below  $10^{15} \text{ cm}^{-3}$  and  $4.2^\circ\text{K}$  mobilities in excess of  $2 \times 10^6 \text{ cm}^2/\text{V-sec}$ .

Photovoltaic detectors have also been fabricated in p-type  $\text{Hg}_{1-x}\text{Cd}_x\text{Te}$  with  $x = 0.50, 0.31$ , and  $0.25$  using proton bombardment to create the n-type layer. Although high-sensitivity photodiodes were obtained with each composition, the best results were obtained with the  $x = 0.31$  material. At  $77^\circ\text{K}$ , these  $15 \times 15\text{-mil}$  diodes had zero-bias impedances of several megohms, peak detectivities at  $3.8\mu$  of  $9 \times 10^{11} \text{ cm}\sqrt{\text{Hz}}/\text{W}$  in reduced background, and peak quantum efficiencies of 29 percent.

Proton bombardment has also been used to fabricate n-p junction photovoltaic detectors in p-type  $\text{PbTe}$ . At  $77^\circ\text{K}$ ,  $5\text{-mil-diameter}$  diodes had zero-bias impedances up to 2 megohms, peak detectivities at  $5\mu$  of  $2.6 \times 10^{11} \text{ cm}\sqrt{\text{Hz}}/\text{W}$  in reduced background, and peak quantum efficiencies of 29 percent.

A separated medium (composite) acoustic surface wave amplifier, using low carrier concentration oxygen-compensated GaAs as the amplifying medium and  $\text{LiNbO}_3$  as the acoustoelectric medium, has shown 10dB of electronic gain at a low operating voltage of  $200\text{V/cm}$ . The large surface depletion regions usually found in high-purity GaAs are greatly reduced in this material, resulting in large acoustoelectric coupling. Expected power dissipation figures for thin crystals of over  $100\text{dB/W}$  are much better than any reported for Si.

A thesis describing the results of both electrical and optical measurements of europium oxide was written during this reporting period.

## II. MATERIALS RESEARCH

A simple technique employing the tri-arc Czochralski furnace has been used to make melting-point measurements on refractory materials at temperatures up to  $2100^\circ\text{C}$ . Comparison of the results with well established values for a number of elements indicates that the measurements are accurate to  $\pm 20^\circ\text{C}$ .

Hall coefficient and resistivity measurements on ZnTe doped with about  $2 \times 10^{20}$  aluminum atoms/cm<sup>3</sup> have been made between 450° and 1000°C under controlled partial pressures of either zinc or tellurium. At these temperatures, low-resistivity n- and p-type behavior was observed at compositions close to zinc and tellurium saturation, respectively.

Previous measurements of the resistivity of  $\text{VO}_x$  as a function of temperature from 300° to 77°K have been extended to liquid helium temperature for samples with  $0.99 \leq x \leq 1.30$ . The results confirm our earlier report that semimetallic behavior is exhibited by samples with  $x < 1.0$ , and semiconducting behavior by those with  $x > 1.0$ .

Conceptual phase diagrams with temperature and the transfer integral  $b$  as coordinates have been constructed for various values of the band occupancy number  $n_f$ . These diagrams have been used in interpreting the magnetic and electrical behavior of a number of pyrites ( $\text{MS}_2$  and  $\text{MSe}_2$ ), including several mixed systems in which  $\text{CoS}_2$  is one end member.

A review of high-pressure synthesis, as illustrated by studies on compounds with the chemical formula  $\text{ABX}_3$  or  $(\text{AX}_n)$  ( $\text{ABX}_3$ ), where A and B are cations and X is an anion, has been prepared for publication as a chapter in Preparative Methods in Solid State Chemistry.

The sources of error in measuring volume compression by means of x-ray diffraction studies at high pressures have been analyzed. The procedures required to obtain accurate lattice parameters for the sample and for a marker material such as NaCl used to determine the applied pressure are discussed in detail.

### III. PHYSICS OF SOLIDS

About twenty magnetoreflexion interband transitions have been observed in the photon energy range 0.5 to 0.30 eV in a very high-quality, extremely homogeneous sample of  $\text{Hg}_{0.839}\text{Cd}_{0.161}\text{Te}$ , which to our knowledge has the highest mobility of any crystal observed to date in this alloy system ( $2.6 \times 10^6 \text{ cm}^2/\text{V-sec}$  at 4.2°K). The data are being used to determine accurate values for the band parameters and their temperature dependence.

Recently, precise determinations of the conduction band parameters in InSb have indicated that the band edge effective mass and g-factor cannot be accurately related by the Roth conduction-valence band  $\vec{k} \cdot \vec{p}$  interaction expression, and a suggestion was made that higher band interactions must be considered. The details of this have been solved by considering the zincblende lattice which is appropriate to InSb as a diamond lattice plus a perturbing antisymmetric potential. The bonding p-like valence band wave functions admix with the higher antibonding p-like conduction band wave functions, and this admixing accounts for the apparent discrepancy.

Polaron self-energy effects in the phonon-assisted cyclotron resonance and in the second-harmonic cyclotron resonance have been observed in InSb for photon energies near twice the known optical phonon energies of InSb. The results indicate unambiguously the existence of a significant electron-TO phonon interaction in a magnetic field.

## Introduction

Polaron studies are also continuing in the silver halides. By using an interferometer and magnetic fields up to 139 kG, Zeeman splitting of photo-induced, bound p-state conduction electrons has been measured in AgBr and AgCl.

Absorption and photoconductivity spectra of hydrogenic donors in high-purity GaAs have been studied using far infrared lasers (HCN, DCN and  $\text{H}_2\text{O}$ ) with resolutions unattainable with conventional techniques. The  $1s \rightarrow 2p$  ( $m = +1$ ) transition is found to consist of three lines; this is believed to be a consequence of differing central cell shifts of the various donors.

A preliminary investigation is under way of the statistical mechanics of a system of electrons on a lattice interacting with each other via intrasite Coulomb repulsion, and with phonons via a Fröhlich interaction. The eigenstates of the system can be obtained, but the evaluation of the partition function of the system has been found to be nontrivial, and the possibility of the existence of a phase transition for the system is under further study.

A theorem has been proven for a many-particle system of either Bosons or Fermions, described by a Hamiltonian  $H$  which is an arbitrary function of creation and annihilation operators. If the eigenstates of  $H$  are denumerable, then a new set of creation and annihilation operators may be defined by an appropriate transformation, such that in the new representation  $H$  is a function of the new Boson or Fermion numbers only. The new operators represent quasiparticles of the many particle system.

Study of the magnetic properties of EuO continues. In addition to determining the magnetic critical indices, the experimental results have been analyzed in terms of the high-temperature series expansion for fcc lattices with nearest ( $J_1$ ) and next-nearest ( $J_2$ ) interactions to determine the value of these interactions. In contrast to previously reported results, based on low-temperature NMR and specific heat which indicate  $J_2/J_1 \approx -0.12$ , we find a ferromagnetic next-nearest neighbor interaction with  $J_2/J_1 = 0.5 \pm 0.2$  and  $J_1/k = 0.53^\circ \pm 0.05^\circ\text{K}$ .

A general treatment has been carried out of the electrodynamic response of a quantum many-electron gas in a nonmagnetic conducting solid immersed in an applied magnetic field with the objective of studying wave propagation and looking for spin effects. Several such interesting spin effects are predicted in the plasma wave properties, both with and without spin-orbit mixing of the one-electron states.

Using a high-power 5- $\mu$  CO laser, inelastic light scattering from plasmons in InSb has been observed for the first time and, by measuring samples of varying doping, the coupled plasmon-phonon modes have been studied. The density and polarization dependence of the scattering indicate that coupling to charge density fluctuations is the dominant scattering mechanism.

Raman scattering has also been carried out in trigonal tellurium with an argon laser. Dispersion arising from the screw symmetry of the lattice has been measured and the phonon symmetries and orderings near the zone center, determined from the Raman scattering selection rules, have been used to obtain the relative contributions of the deformation potential and the electro-optic effect to the electron-phonon interaction.



The Green's function method has been applied to the polaron coupling of an  $n = 2$  and  $n = 1$  Landau level of an electron in a magnetic field when the cyclotron frequency is close to the LO phonon frequency. Because of the simultaneous coupling of the  $n = 1$  and  $n = 0$  Landau levels, it is found that Raman scattering, resulting in the excitation of electrons from the  $n = 0$  to  $n = 2$  Landau level, will exhibit the effect of  $n = 2$  and  $n = 1$  level coupling.

Nonlinear mixing in GaAs of two millimeter or submillimeter signals has been analyzed for the case when the difference frequency is detected in the photocurrent. Important mechanisms at low difference frequencies seem to be carrier density modulation due to the energy dependence of the carrier lifetime and of the energy relaxation time, and carrier density modulation due to the nonlinearity of the photoexcitation of the donor states by the submillimeter sources.

#### IV. MICROELECTRONICS

Aluminum beam leaded devices have been fabricated and assembled with good results. Ultrasonic bonding of the beam lead chips to appropriate substrates has required considerable study and evaluation, and will continue as a development program.

Beam lead substrates of the flexible type with aluminum beam leads are being fabricated using material from several sources. Some difficulties exist in obtaining laminated aluminum polyimide sheets with appropriate properties, particularly in terms of the aluminum. Early efforts on thick aluminum resulted in severe undercutting during the etching process and, more recently, thinner aluminum has not exhibited the characteristics required for good bonding.

A new bonding method, ultrasonic ball bonding, for the general fabrication of hybrid circuits, has been implemented which eliminates elevated temperatures during the assembly period.

The laser scanner program for the evaluation of semiconductor devices has progressed sufficiently so that accurate device gain can be measured using the laser as an input.

The semiconductor clean room is operational and, although there are some remaining modifications to be made before it meets the original specifications, we expect to be able to process components within eight weeks.

Computer-aided mask making has temporarily been interrupted in order to relocate the photogenerator and photorepeater in a more suitable environment. The techniques for processing masks at micron and submicron line widths will be explored in greater detail when the area is operational again.

# CONTENTS

Abstract	iii
Introduction	iv
Organization	x
Reports by Authors Engaged in Solid State Research	xi
 I. SOLID STATE DEVICE RESEARCH	 1
A. Long-Wavelength Infrared $\text{Hg}_{1-x}\text{Cd}_x\text{Te}$ Photovoltaic Detectors	1
B. Mass Transfer Induced Liquid State Crystal Growth and Temperature Gradient Annealing of $\text{Hg}_{1-x}\text{Cd}_x\text{Te}$	2
C. Type Conversion and n-p Junction Formation in $\text{Hg}_{1-x}\text{Cd}_x\text{Te}$ Produced by Proton Bombardment	4
D. Type Conversion and n-p Junction Formation in PbTe Produced by Proton Bombardment	8
E. A Low-Power Density GaAs/LiNbO <sub>3</sub> Surface Wave Amplifier	10
F. Conductivity Studies in Europium Oxide	12
 II. MATERIALS RESEARCH	 15
A. Melting Point Measurements in the Tri-Arc Furnace	15
B. Carrier Concentration and Mobility in n- and p-Type ZnTe:Al	17
C. Semiconducting and Semimetallic Behavior in VO	21
D. Conceptual Phase Diagram and Its Application to the Spontaneous Magnetism of Pyrites	23
E. Volume Compression Measurements by X-Ray Diffraction Studies at High Pressures	26
 III. PHYSICS OF SOLIDS	 33
A. Electronic Band Structure	33
1. Interband Magnetoreflexion of $\text{Hg}_{0.839}\text{Cd}_{0.161}\text{Te}$	33
2. Conduction Band Parameters for InSb	33
3. Polaron Self-Energy Effects in the Phonon-Assisted Cyclotron Resonance and the Second-Harmonic Cyclotron Resonance of InSb	35
4. Polaron Zeeman Effects in the Silver Halides	36
5. Laser Magnetospectroscopy in GaAs	37
6. Lattice Effects in the Localized State	41
7. Existence of Exact Quasi-Particles for Systems of Interacting Particles	42

B. Magnetism	45
1. Magnetic Properties of EuO	45
2. Electron Spin Waves in Nonmagnetic Conductors: Self-Consistent Field Theory	45
C. Laser Scattering and Nonlinear Effects	46
1. Light Scattering from Plasmons in InSb	46
2. Raman Scattering and Lattice Dynamics of Tellurium	47
3. Resonant Coupling of Landau Levels via LO Phonons in Polar Semiconductors and Its Effect on Landau Level Raman Scattering from Semiconductor Plasmas	49
4. Two-Wave Nonlinear Mixing in GaAs	49
IV. MICROELECTRONICS	53
A. Low TCR Tantalum Nitride Resistors	53
B. Aluminum Interconnections and Beam Leads on Polyimide Substrates	53
C. Computer-Aided Design (CAD) and Mask Facility	54

# ORGANIZATION

## SOLID STATE DIVISION

A. L. McWhorter, *Head*  
P. E. Tannenwald, *Associate Head*  
C. R. Grant, *Assistant*

### SOLID STATE THEORY

H. J. Zeiger, *Leader*  
M. M. Litvak, *Assistant Leader*

Bari, R. A.	Lao, B. Y. <sup>†</sup>
Brine, N. S.	Larsen, D. M.
Brodersen, R. W.*	Ngai, K. L.
Davies, R. W.	Palm, B. J. <sup>‡</sup>
Dresselhaus, G. F.	Sommerfeldt, E. <sup>†</sup>
Kaplan, T. A.	Wilson, A. R. M.
Landon, S. N.	Young, C. Y.

### ELECTRONIC MATERIALS

J. B. Goodenough, *Leader*  
A. J. Strauss, *Associate Leader*

Anderson, C. H., Jr.	Longo, J. M.
Banus, M. D.	Mastromattei, E. L.
Batson, D. A.	Owens, E. B.
Brebrick, R. F., Jr.	Pantano, J. V.
Button, M. J.	Pierce, J. W.
Capes, R. N., Jr.	Plonko, M. C.
Delaney, E. J.	Racchah, P. M.
England, R. E.	Reed, T. B.
Fahey, R. E.	Roddy, J. T.
Finn, M. C.	Searles, I. H.
Iseler, G. W.	Smith, F. T. J.
Kafalas, J. A.	Stack, T. E.
LaFleur, W. J.	Steininger, J. M.
Lavine, M. C. <sup>‡</sup>	Temkin, R. J.*
Leyenaar, A. R.	Tracy, D. M.

### MICROELECTRONICS

R. E. McMahon, *Leader*

Bachner, F. J.	McBride, W. F.
Beatrice, P. A.	McGonagle, W. H.
Childs, N. B.	Mountain, R. W.
Cohen, R. A.	Pichler, H. H.
Durant, G. L.	Pybus, V. J.
Grant, L. L.	Smythe, D. L. <sup>†</sup>
Gray, R. V.	Wilde, R. E.

### SOLID STATE PHYSICS

J. G. Mavroides, *Leader*  
G. B. Wright, *Assistant Leader*

Allen, J. W.	Henrich, V. E.
Barch, W. E.	Johnson, E. J.
Blum, F. A., Jr.	Kernan, W. C.
Brandt, R. C.	Kolesar, D. F.
Burke, J. W.	Melngailis, J.
Chinn, S. R.	Menyuk, N.
DeFeo, W. E.	Nill, K. W.
Dresselhaus, M. S. <sup>‡</sup>	Parker, C. D.
Dwight, K., Jr.	Pine, A. S.
Feldman, B.	Scouler, W. J.
Fetterman, H.	Strahm, N.
Glassbrenner, C. J. <sup>†</sup>	Waldman, J.*
Groves, S. H.	Weber, R.

### APPLIED PHYSICS

J. O. Dimmock, *Leader*  
T. C. Harman, *Assistant Leader*  
I. Melngailis, *Assistant Leader*

Belanger, L. J.	Lindley, W. T.
Brueck, S. R. J.*	Mooradian, A.
Calawa, A. R.	Murphy, R. A.*
Carter, F. B.	Oliver, M. R. <sup>†</sup>
Caswell, F. H.	Orphanos, W. G.
Clough, T. F.	Paladino, A. E.
Donnelly, J. P.	Rossi, J. A.
Ferrante, G. A.	Spears, D. L.
Foyt, A. G.	Stillman, G. E.
Hancock, R.	Ward, J. H. R., III
Holcomb, T. <sup>†</sup>	Wolfe, C. M.
Hurwitz, C. E.	Woods, R. J.
Krohn, L., Jr.	Youtz, P.

### MICROSOUND

E. Stern, *Leader*

Alusow, J. A.	Hawrylok, R. <sup>†</sup>
Brogan, W. T.	Smith, H. I.
Burke, B. E.	Waldron, R. A.
Chen, F.	Williamson, R.

---

\* Research Assistant

† Summer Staff

‡ Part Time



# REPORTS BY AUTHORS ENGAGED IN SOLID STATE RESEARCH

15 May through 15 August 1970

## PUBLISHED REPORTS

		<u>Journal Articles*</u>	
JA No.			
3429A	Avalanche Breakdown and Light Emission at Low-Angle Boundaries in n-ZnSe	J.P. Donnelly F.T.J. Smith	Solid-State Electron. <u>13</u> , 516 (1970), DDC AD-708604
3499	Infrared Cyclotron Resonance and Related Experiments in the Conduction Band of InSb	E.J. Johnson D.H. Dickey	Phys. Rev. B <u>1</u> , 2672 (1970)
3546	Transport Equation for a Fermi System in Random-Scattering Centers. II. Independent Electrons in an Arbitrarily Varying Electric Field and Strong Single-Center Potentials	J.L. Sigel P.N. Argyres†	Phys. Rev. B <u>1</u> , 1845 (1970)
3552	Resistivity, Magnetoresistance, and Hall Effect Studies in $\text{VO}_x$ ( $0.82 \leq x \leq 1.0$ )	J.M. Honig† W.E. Wahnsiedler† M.D. Banus T.B. Reed	J. Solid State Chem. <u>2</u> , 74 (1970)
3553	MIS Electroluminescent Diodes in ZnTe	J.P. Donnelly A.G. Foyt W.T. Lindley G.W. Iseler	Solid-State Electron. <u>13</u> , 755 (1970)
3557	Hall Coefficient Factor for Polar Mode Scattering in n-Type GaAs	G.E. Stillman C.M. Wolfe J.O. Dimmock	J. Phys. Chem. Solids <u>31</u> , 1199 (1970)
3563	Interdiffusion in Lead Selenide	R.W. Brodersen† J.N. Walpole† A.R. Calawa	J. Appl. Phys. <u>41</u> , 1484 (1970)
3579	Photoluminescence Due to Isoelectronic Oxygen and Tellurium Traps in II-VI Alloys	G.W. Iseler A.J. Strauss	J. Luminescence <u>3</u> , 1 (1970)
3582	Interpretation of $\text{M}_x\text{V}_2\text{O}_5$ - $\beta$ and $\text{M}_x\text{V}_{2-y}\text{T}_y\text{O}_5$ - $\beta$ Phases	J.B. Goodenough	J. Solid State Chem. <u>1</u> , 349 (1970)

---

\* Reprints available.

† Author not at Lincoln Laboratory.

# Reports

JA No.

3590	Thermodynamics and Calculation of the Liquidus-Solidus Gap in Homogeneous, Monotonic Alloy Systems	J.M. Steininger	J. Appl. Phys. <u>41</u> , 2713 (1970)
3592	Structure and Magnetic Properties of $\text{VO}_2$	J.M. Longo R.J. Arnott*	J. Solid State Chem. <u>1</u> , 394 (1970)
3601	Structure of the $\text{M}_x\text{V}_2\text{O}_5-\beta$ and $\text{M}_{x/2-y}\text{V}_{2-y}\text{O}_5-\beta$ Phases	J. Galy* J. Darriet* A. Casalot* J.B. Goodenough	J. Solid State Chem. <u>1</u> , 339 (1970)
3602	Laser Raman Spectroscopy	A. Mooradian	Science <u>169</u> , 20 (1970)
3603A	Simple Model Potential Approach to the X-Ray Form Factor in Aluminium	P. Ascarelli* P.M. Raccach	Phys. Letters <u>31A</u> , 549 (1970)
3610	Localized One-Electron States in Perfect Crystals as a Consequence of the Thermal Single-Determinant Approximation	T.A. Kaplan P.N. Argyres*	Phys. Rev. B <u>1</u> , 2457 (1970)
3626	Simple, Versatile Techniques for Qualitative and Quantitative Evaluation of Spark Source Mass Spectrographic Plates	E.B. Owens	Rev. Sci. Instr. <u>41</u> , 636 (1970)
3628	Electronic Structure of Palladium	F.M. Mueller* A.J. Freeman* J.O. Dimmock A.M. Furdyna*	Phys. Rev. B <u>1</u> , 4617 (1970)
3633	Electron Mobility in High-Purity GaAs	C.M. Wolfe G.E. Stillman W.T. Lindley	J. Appl. Phys. <u>41</u> , 3088 (1970)
3645	Report on the Symposium on Magnetic Semiconductors, IBM Research Center, Yorktown Heights, N.Y.	J.B. Goodenough	Phys. Today <u>23</u> , 79 (1970)
3646	Quantitative Analysis of Ternary and Quaternary Semiconducting Alloys with the Electron Microprobe	M.C. Finn	Analytical Chem. <u>42</u> , 1084 (1970)
3648	n-p Junction Photodetectors in InSb Fabricated by Proton Bombardment	A.G. Foyt W.T. Lindley J.P. Donnelly	Appl. Phys. Letters <u>16</u> , 335 (1970)
3651A	Anomalous Absorption of Microwaves by Interstellar $\text{H}_2\text{CO}$	M.M. Litvak	Astrophys. J. <u>160</u> , L133 (1970)

---

\* Author not at Lincoln Laboratory.

JA No.

- |      |  |  |  |
|------|--|--|--|
| 3657 | X-Ray Diffraction at High Pressures (A Review)   | M.D. Banus   | High Temperatures-High Pressures <u>1</u> , 483 (1969) |
| 3672 | Laser Emission from Metal-Semiconductor Barriers on PbTe and $\text{Pb}_{0.8}\text{Sn}_{0.2}\text{Te}$ | K.W. Nill<br>A.R. Calawa<br>T.C. Harman<br>J.N. Walpole* | Appl. Phys. Letters <u>16</u> , 375 (1970)             |
| 3681 | Ultrasonic Attenuation Near the Spin-Alignment Transition of EuTe                                      | Y. Shapira*<br>T.B. Reed                                 | Phys. Letters <u>31A</u> , 381 (1970)                  |
| 3701 | Analysis of Frozen Aqueous Solutions by Spark Source Mass Spectroscopy                                 | E.B. Owens   | Analytical Letters <u>3</u> , 223 (1970)               |
| 3721 | Seebeck Coefficients in Vanadium Spinel  | J.B. Goodenough  | Materials Res. Bull. <u>5</u> , 621 (1970)             |

MS No.

- |      |  |  |  |
|------|--|--|--|
| 2610 | The Physics and Technology of Surface Elastic Waves                  | H.I. Smith                                 | Int'l. J. Nondestructive Testing <u>2</u> , 31 (1970)  |
| 2683 | Temperature and Magnetic Field Dependence of the Conductivity of EuO | M.R. Oliver<br>J.O. Dimmock<br>T.B. Reed   | IBM J. Res. Develop. <u>14</u> , 276 (1970)  |
| 2708 | Optical Properties of the Europium Chalcogenides                     | J.O. Dimmock                               | IBM J. Res. Develop. <u>14</u> , 301 (1970)  |
| 2778 | N-P Junction Photodetector in InSb Fabricated by Proton Bombardment  | A.G. Foyt<br>W.T. Lindley<br>J.P. Donnelly | Proceedings Detector Specialty Group Meeting, Santa Barbara, California, 12-13 February 1970 (Willow Run Laboratories, University of Michigan, 1970), p.129. |

\* \* \* \* \*

UNPUBLISHED REPORTS

Journal Articles

JA No.

- |      |  |   |                        |
|------|--|---|------------------------|
| 3539 | Positron Annihilation in Copper - Comparisons of Different Results | J. Melngailis                           | Accepted by Phys. Rev. |
| 3631 | Electrical Conductivity in Narrow Energy Bands                     | R. A. Bari<br>D. Adler*<br>R. V. Lange* | Accepted by Phys. Rev. |

---

\* Author not at Lincoln Laboratory.

## Reports

JA No.

3659A	Direct Observation of Acoustical Activity in $\alpha$ -Quartz	A. S. Pine	Accepted by Phys. Rev.
3664	Magnetoreflexion Studies in Bismuth	M. Maltz* M. S. Dresselhaus	Accepted by Phys. Rev.
3678A	Rigid and Nonrigid Beam Lead Substrates	F. J. Bachner R. A. Cohen R. E. McMahon	Accepted by Solid State Tech.
3682	Narrow-Band Expansions in the Hubbard Model: A Comment	R. A. Bari	Accepted by Phys. Rev.
3687	Phase Diagram of the CdTe-CdSe Pseudobinary System	A. J. Strauss J. M. Steininger	Accepted by J. Electrochem. Soc.
3716	Phase Diagram of the PbTe-PbSe Pseudobinary System	J. M. Steininger	Accepted by Metallurgical Trans.
3727	Linewidths of a Gaussian Broadband Signal in a Saturated Two-Level System	M. M. Litvak	Accepted by Phys. Rev.
3730	Si <sub>3</sub> N <sub>4</sub> Masked, Thermally Oxidized, Post Diffused Mesa Process (SIMTOP)	R. A. Cohen R. W. Mountain	Accepted by IEEE Trans. Electron Devices
3737	Study of the Spin-Reordering Transition in Cr <sub>5</sub> S <sub>6</sub>	K. Dwight N. Menyuk J. A. Kafalas	Accepted by Phys. Rev.
3738	Effects of Hydrostatic Pressure and of Jahn-Teller Distortions on the Magnetic Properties of RbFeF <sub>3</sub>	J. B. Goodenough N. Menyuk K. Dwight J. A. Kafalas	Accepted by Phys. Rev.

## Meeting Speeches<sup>†</sup>

MS No.

2571B	Ion Implantation in Compound Semiconductors	A. G. Foyt	Seminar, Fairchild Semiconductor Div., Palo Alto, California, 4 June 1970
2667A	A Gridded Thick Film Metallization Structure Employed in a Multichip Circuit Fabrication	H. H. Pichler	NEPCON '70 East, 16-18 June 1970
2891	Optical Properties of the Alkalis Using the KKR-Z Method	A. R. Wilson G. Dresselhaus C. Y. Young	Conference on the Computational Methods in Band Theory, IBM, Yorktown Heights, New York, 14-15 May 1970

\* Author not at Lincoln Laboratory.

† Titles of Meeting Speeches are listed for information only. No copies are available for distribution.



MS No.

2898	Interstellar Molecular Masers	M.M. Litvak	Columbia Radiation Laboratory Seminar, Columbia University, 29 May 1970
2901	Type Conversion and n-p Junction Formation in $\text{Hg}_{1-x}\text{Cd}_x\text{Te}$ Produced by Proton Bombardment	A.G. Foyt T.C. Harman J.P. Donnelly	Electronic Device Research Conference, Seattle, Washington, 29 June - 2 July 1970
2903	A New Technique for the Fabrication of GaAs Schottky Barrier Field Effect Transistors	W.T. Lindley C.E. Hurwitz A.G. Foyt	
2906	Growth of Oxide Crystals	T.B. Reed	International Conference on Ferrites, Kyoto, Japan, 6-10 July 1970
2922	Beam Lead Packaging	R.E. McMahon	Eastern Electronics Packaging Conference, M.I.T., 8-9 June 1970
2932	Theory of Chemical Diffusion in Ceramics	R.F. Brebrick	Materials Seminar, Aerospace Research Laboratories, Wright-Patterson Air Force Base, Dayton, Ohio, 25 June 1970
2957	Electrical Characterization of II-VI Semiconductor Compounds	F.T.J. Smith	Summer Course on Characterization of Electronic Materials, M.I.T., 3 August 1970
2965	Experiments on Bound Polarons in the Silver Halides	R.C. Brandt	Seminar, Eastman Kodak, Rochester, New York, 5 August 1970
2968	The Characterization of Electronic Materials by Means of Schottky Barrier Diodes	W.T. Lindley	Seminar, Department of Metallurgy and Materials Sciences, M.I.T., 3-4 August 1970
2969	Hall Effect and Extrinsic Photoconductivity Measurements: GaAs	G.E. Stillman	

## I. SOLID STATE DEVICE RESEARCH

### A. LONG-WAVELENGTH INFRARED $\text{Hg}_{1-x}\text{Cd}_x\text{Te}$ PHOTOVOLTAIC DETECTORS

Photovoltaic detectors have been fabricated from small-bandgap  $\text{Hg}_{1-x}\text{Cd}_x\text{Te}$  crystals by Hg-diffusion and have been tested at wavelengths up to  $48\mu$  at  $4.2^\circ\text{K}$ . The starting material was p-type  $\text{Hg}_{1-x}\text{Cd}_x\text{Te}$  grown by a new method described in Sec. 1-B. Most of the results were obtained using a crystal which had an alloy composition  $x = 0.179$  (determined by electron microprobe measurements), a hole concentration of  $1.5 \times 10^{17} \text{ cm}^{-3}$ , and a hole mobility of  $415 \text{ cm}^2 \text{ V}^{-1} \text{ sec}^{-1}$  at  $77^\circ\text{K}$ . The crystal was etch-polished and then free-etched using a 1.5-percent bromine-methanol solution. A  $60\text{-}\mu$  deep n-type layer was formed on the p-type substrate by diffusion in an evacuated ampoule at  $320^\circ\text{C}$  for 3 hours using a Hg-source. Contact to the entire p-side of the wafer was made by plating a layer of gold followed by a layer of indium. Small circular contacts were made to the n-side by plating indium. Several detector elements were formed on the same wafer by masking and etching out mesa-structures about 1 mm in diameter on the n-side of the wafer. All experiments were made with the diodes immersed in liquid helium.

The observed spectral response shown in Fig. 1-1 has a strong peak prior to the cutoff which occurs at about  $35\mu$ . The quantum efficiency at the peak is estimated at 7 percent for the diode which had a sensitive area of  $1.4 \times 10^{-2} \text{ cm}^2$  and a zero-bias impedance of 80 ohms. The reduced efficiency and the strongly peaked response is expected to be due to recombination losses in the  $60\text{-}\mu$  thick n-type layer. A noise voltage of  $1.2 \times 10^{-9} \text{ V}/\sqrt{\text{Hz}}$  was measured at a frequency of 1 kHz and  $2.4 \times 10^{-10} \text{ V}/\sqrt{\text{Hz}}$  at 5 kHz. These values can be compared with a calculated thermal noise voltage of  $1.3 \times 10^{-10} \text{ V}/\sqrt{\text{Hz}}$  for the 80-ohm impedance at  $4.2^\circ\text{K}$ . The origin of the frequency-dependent excess noise is uncertain at present. By using the measured value of noise voltage at 1 kHz, a detectivity of about  $1 \times 10^{10} \text{ cm}\sqrt{\text{Hz}}/\text{W}$  is estimated at a wavelength of  $30\mu$ . Although there was a variation in the zero-bias impedance of diodes on the same wafer, such that the lowest impedance was about one-third of the impedance for the above diode, the cutoff wavelength for diodes on a  $0.5 \times 0.5\text{-cm}$  wafer was identical within the resolution of the spectrometer, which was better than  $0.5\mu$ . This provides evidence that these crystals are very homogeneous with respect to their Hg-to-Cd ratio.

Diodes fabricated in a similar manner from a smaller bandgap crystal with a composition  $x = 0.171$  had photoresponse out to the wavelength limit of  $48\mu$  for the spectrometer used.

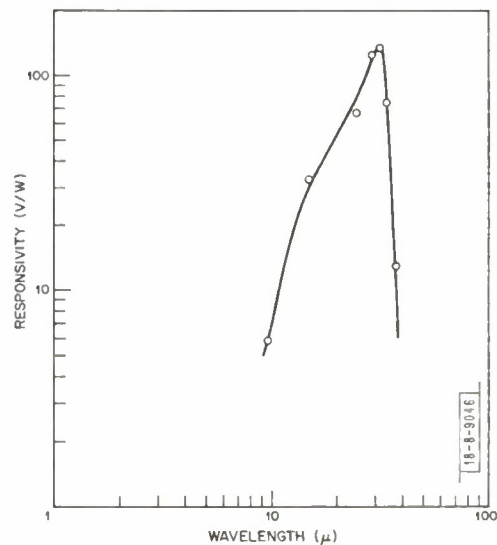


Fig. 1-1. Responsivity spectrum of  $\text{Hg}_{0.821}\text{Cd}_{0.179}\text{Te}$  photovoltaic detector of  $4.2^\circ\text{K}$ .

I. Melngailis  
T. C. Harman

## Section I

### B. MASS TRANSFER INDUCED LIQUID STATE CRYSTAL GROWTH AND TEMPERATURE GRADIENT ANNEALING OF $\text{Hg}_{1-x}\text{Cd}_x\text{Te}$

It has been found that unusually high-quality  $\text{Hg}_{1-x}\text{Cd}_x\text{Te}$  crystals can be obtained by using a new technique for crystal preparation. For a number of years, it has been known that the problem of preparing high-quality single crystals of pseudobinary semiconducting alloys is rather formidable, particularly in the case<sup>1-3</sup> of  $\text{Hg}_{1-x}\text{Cd}_x\text{Te}$ . In Refs. 1 and 2, a very slow growth rate, large temperature gradient Bridgman technique was used, whereas in Ref. 3, a two-step technique employing a quench from the liquid state followed by an anneal below the melting point was adopted. In this section, a third method will be discussed.

If a pseudobinary alloy system  $\text{M}_{1-x}\text{N}_x\text{T}$  forms solid solutions, at least, in the compositional range of  $x = a$  to  $x = c$  [see Fig. I-2(a)], and if a solid alloy of initial composition  $x = b$  and a liquid alloy of initial composition  $x = b$  are placed in contact with each other in a temperature gradient, then three separate regions will form [see Fig. I-2(b)]. At temperature  $T_B$  and

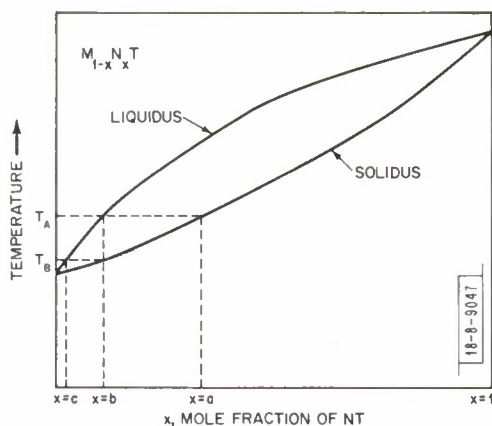


Fig. I-2(a). Phase diagram for arbitrary pseudo-binary MT-NT system.

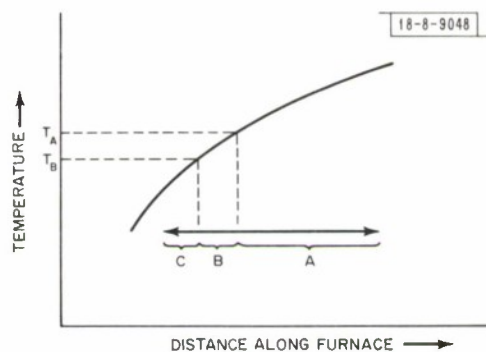


Fig. I-2(b). Designation of position of charge, liquid fraction (Region A) and solid fraction (Regions B and C) after steady state is achieved.

for lower temperatures, only solid of composition  $x = b$  should be present [Region C of Fig. I-2(b)]. At temperature  $T_A$  and above, only liquid of composition  $x = b$  will be present [Region A of Fig. I-2(b)]. Between Regions A and C, a region (Region B) composed of a mixture of liquid and solid (slush) should occur with an overall average initial composition of  $x = b$ . If local equilibrium is assumed for Region B, then at the solid-slush (C-B) interface, solid with  $x = b$  will be in local equilibrium with slush composed of a mixture of liquid with  $x = c$  and solid with  $x = b$ . Also, at the slush-liquid (B-A) interface, liquid with  $x = b$  will be in local equilibrium with slush composed of a mixture of liquid with  $x = b$  and solid with  $x = a$ . Due to thermal diffusion, concentration diffusion, and convective mixing in the liquid, mass transfer of NT from the liquid Region A into the slush Region B will occur. It is assumed that the volume of the solid plus slush fractions is small compared with the volume of liquid fraction. Further, diffusion in the solid is assumed to be a relatively small effect. The eventual effect of the enhanced NT components of the alloy in Region B will be to increase  $x$  in the liquid part of the slush at



the solid-slush interface. As  $x$  in the liquid increases at the solid-slush interface, crystal growth will occur, i.e., solid with  $x > b$  freezes out at the solid-slush interface, which causes the interface to move. It is observed experimentally that the solid composition increases very rapidly, approaching  $x \approx a$  in a few millimeters. On the basis of the above model, it is believed that the crystal growth process will continue until a macroscopic steady state has been reached, at which time the slush region should have converted to crystalline solid. One possible unique advantage in crystal growth from a mixture of solid particles in intimate contact with liquid is that equilibrium in the vicinity of the growing interface may be approached quite closely. Also, the thermal and hydrodynamic stability may be enhanced at the growing interface, since convective flow is expected to be reduced.

Further, if the charge is annealed for a long time in the same imposed temperature gradient, then stoichiometric excesses of M-N or T in the form of inclusions may migrate from the solid of Region B to the liquid of Region A by the principle of temperature gradient zone melting.<sup>4</sup> At present, the above technique, which involves mass transport induced liquid state crystal growth and simultaneous temperature gradient annealing very near the melting point, has been applied only to the  $\text{Hg}_{1-x}\text{Cd}_x\text{Te}$  pseudobinary system as described below. However, the method is anticipated to be applicable to other pseudobinary alloy systems, such as  $\text{Pb}_{1-x}\text{Sn}_x\text{Te}$  and  $\text{Pb}_{1-x}\text{Sn}_x\text{Se}$ .

In the procedure for the preparation of  $\text{Hg}_{1-x}\text{Cd}_x\text{Te}$  based on the above method, the steps described in Ref. 1 were used to achieve a completely molten charge of  $\text{Hg}_{0.94}\text{Cd}_{0.06}\text{Te}$  in a vertically positioned quartz ampoule at a temperature above  $T_A$ . Hydrodynamic and thermal stability<sup>5</sup> are enhanced by growing the crystal vertically upward. Then, the tube is quickly lowered to a new position in the furnace such that part of the 200-g charge was quick-frozen solid, part slush and part liquid with an imposed temperature gradient of about  $10^\circ\text{C}/\text{cm}$  at the liquid-solid interface. After a crystal-growing and annealing time of 44 days, the ingot is furnace-cooled to room temperature. Upon extensive metallographic characterization of numerous slices cut from ingots, three distinct regions are identified in agreement with the above concept. In Region C, the CdTe content was found to vary randomly about composition  $x \approx 0.06$  ( $x \approx b$ ). Region A was quite polycrystalline and obviously was frozen quickly from the liquid state during the furnace-cool final step of the experiment. For Region A, the CdTe content was found to vary randomly about composition  $x \approx 0.06$ . Region B (1 cm in length) was found to be a high-quality single crystal of approximate composition  $x \approx 0.18$  ( $x \approx a$ ). Specimens 0.75 mm in thickness cut from Region B are found to be homogeneous with respect to the Cd-Hg ratio (to within the accuracy of the electron microprobe) over the 1.8-cm-diameter sample surfaces. A small longitudinal compositional gradient is observed along most of the length. However, a large compositional gradient ( $x = 0.063$  to  $x = 0.106$  in 0.75 mm) is found near the Region C - Region B interface, which is consistent with a large change in liquidus composition during the early stages of growth as anticipated from the model.

The as-grown crystals are p-type with carrier concentrations in the  $2$  to  $3 \times 10^{17}/\text{cm}^3$  range. The source of the carriers is believed to be due to metal vacancy point defects. In order to minimize the defects, samples are annealed in mercury vapor at low temperatures as indicated in Table I-1. After annealing, the specimens are n-type with carrier concentrations in the  $10^{14}/\text{cm}^3$  to  $10^{15}/\text{cm}^3$  range. Evidence for the unusually high quality (low density of crystalline



TABLE I-1 ANNEALED SAMPLES OF $\text{Hg}_{1-x}\text{Cd}_x\text{Te}$ GROWN BY THE NEW METHOD					
Sample No.	Mole Fraction $\text{CdTe}$ (x)	Hg-Annealing Temperature (°C)	Annealing Time (days)	Carrier Concentration at 4°K ( $\text{cm}^{-3}$ )	Carrier Mobility at 4°K ( $\text{cm}^2/\text{V-sec}$ )
1A	0.181	240	4	$1.5 \times 10^{15}$	$1.1 \times 10^6$
6D	0.161	240	4	$9.4 \times 10^{14}$	$2.6 \times 10^6$
11D	0.15	420	3	$5.0 \times 10^{14}$	$1.6 \times 10^6$

imperfections) of the annealed crystals is indicated from the electron carrier mobilities as given in Table I-1. At the present time, the electron mobility of  $2.6 \times 10^6 \text{ cm}^2/\text{V-sec}$  represents the highest value reported for  $\text{Hg}_{1-x}\text{Cd}_x\text{Te}$ . It is noted that the mobility values in Table I-1 are in satisfactory agreement with the theoretical electron mobility curve given by Long.<sup>6</sup> Additional evidence for the unusual quality of the material is indicated by the quality of the magnetoreflectivity data, which are comparable to the best obtained for InSb and grey Sn (see Sec. III-A-1 of this report).

T. C. Harman

#### C. TYPE CONVERSION AND n-p JUNCTION FORMATION IN $\text{Hg}_{1-x}\text{Cd}_x\text{Te}$ PRODUCED BY PROTON BOMBARDMENT

We have found that proton bombardment can be used to convert p-type  $\text{Hg}_{1-x}\text{Cd}_x\text{Te}$  into n-type, and have used this technique to fabricate n-p junction photovoltaic detectors in this material. Although diode detectors can be made in  $\text{Hg}_{1-x}\text{Cd}_x\text{Te}$  using diffusion techniques,<sup>7-9</sup> our results indicate that the bombardment technique offers an attractive and convenient alternative method of making high-sensitivity detectors in this material. One important feature of this technique is that all the sample processing can be done at temperatures less than 60°C. In this section, the device fabrication technique is described and an electrical and photovoltaic evaluation of the diodes is presented.

Three crystals of p-type  $\text{Hg}_{1-x}\text{Cd}_x\text{Te}$  with different compositions were used in these experiments. Crystal A was grown by the new method described in the previous section of this report, whereas crystals B and C were grown using the modified Bridgman technique.<sup>1</sup> Table I-2 gives the composition, energy gap at the detector operating temperature, hole carrier concentration and mobility in the bulk, and the proton bombardment energy and dose used for each crystal. Samples were prepared from these crystals using standard cutting and lapping techniques. Each sample was etched for 30 sec in a 20-percent bromine-methanol solution, and rinsed in methanol. An array of 3-mil-diameter gold contacts on 10-mil centers was then plated onto the top surface of the sample using photoresist as a plating mask. These contacts were sufficiently thin ( $\sim 500 \text{ \AA}$ ) that they were easily penetrated by the proton beam. The initial photoresist layer was then removed, and a thick layer of photoresist ( $\sim 10 \mu$  thick) was applied to the top surface of the sample.

TABLE I-2 SOME SALIENT FEATURES OF $\text{Hg}_{1-x}\text{Cd}_x\text{Te}$ CRYSTALS			
	Sample A	Sample B	Sample C
x	0.5	0.31	0.25
Energy gap (eV)	0.6 (300°K)	0.3 (77°K)	0.18 (77°K)
Carrier concentration p ( $10^{16} \text{ cm}^{-3}$ )	1.3 (300°K)	2.5 (77°K)	7 (77°K)
Hole mobility $\mu$ ( $\text{cm}^2/\text{V-sec}$ )	50 (300°K)	250 (77°K)	330 (77°K)
Proton energy (keV)	100	200	200
Proton dose ( $\text{cm}^{-2}$ )	$1.6 \times 10^{14}$	$2 \times 10^{14}$	$5 \times 10^{14}$

Finally, 15-mil-square holes were opened in the photoresist layer to define the areas to be bombarded. This layer is sufficiently thick to stop the proton beam from reaching the sample. Consequently, only those areas from which the photoresist was removed were exposed to the proton beam. The sample was then placed in the ion accelerator, a portion of it was bombarded with protons, and it was then removed from the accelerator for electrical evaluation. A sketch of the final bombarded configuration is shown in Fig. I-3.

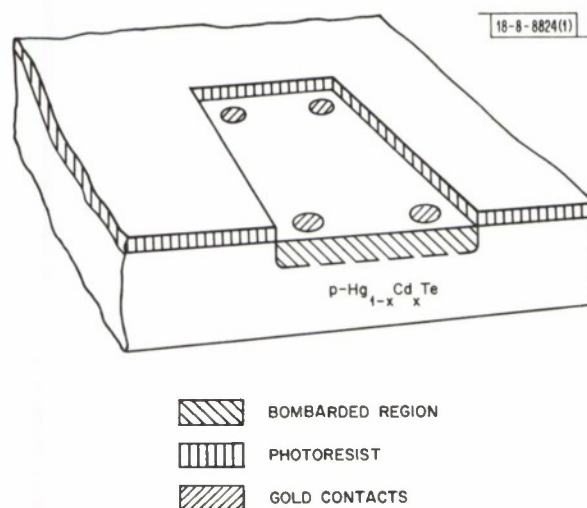


Fig. I-3. Sketch of  $\text{Hg}_{1-x}\text{Cd}_x\text{Te}$  n-p junction photo-voltaic detector in which proton bombardment was used to fabricate n-type layer.

## Section I

The first experiments were done using samples from crystal A, which were bombarded with 100-keV protons as noted in Table I-2. As an initial electrical evaluation, we performed van der Pauw style Hall effect measurements<sup>10</sup> using the four contacts on a bombarded square, and repeated the measurement using four contacts on an unbombarded square. These measurements showed that the bombarded region had been converted to n-type material, whereas the substrate remained p-type. At room temperature, the n-type bombarded layer, which was about  $1\ \mu$  thick, had a carrier concentration of about  $10^{17}/\text{cm}^3$  and an electron mobility of  $1000\ \text{cm}^2/\text{V-sec}$ . As a further test, we measured the current-voltage characteristics between the various contacts. Between two contacts on a bombarded square, a linear current-voltage characteristic was seen, with a resistance of about 800 ohms. Between two contacts on an unbombarded square, linear characteristics were also observed, with a resistance of 1000 ohms. However, between a contact on a bombarded square and a contact on an unbombarded square or on the substrate, we observed diode characteristics. The current-voltage characteristic for one of these diodes is illustrated in Fig. I-4. The device exhibits a normal junction diode characteristic, with a zero-bias resistance of about 200 kohms in the dark. Also shown is the characteristic with a microscope light shining on the diode to illustrate that it exhibits a normal photovoltaic response.

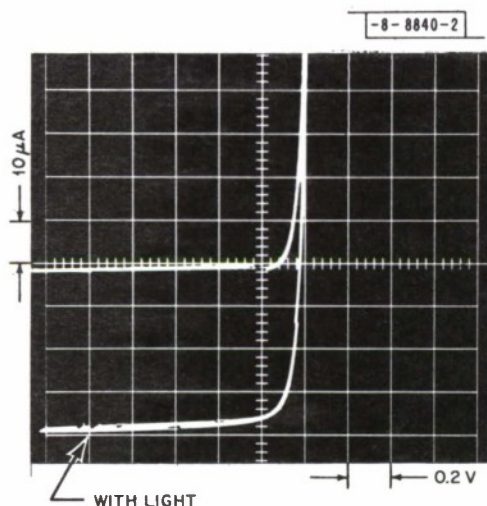


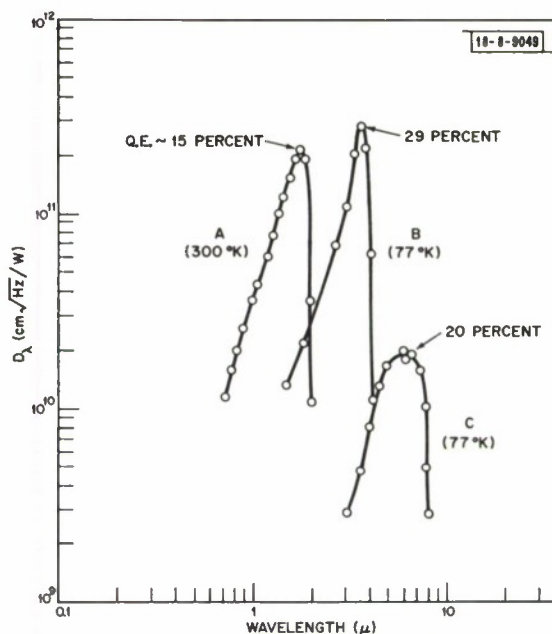
Fig. I-4. Current-voltage characteristic of  $15 \times 15$ -mil square photovoltaic detector in  $\text{Hg}_{0.5}\text{Cd}_{0.5}\text{Te}$ , in which n-type layer was made using proton bombardment. Diode is at  $300^\circ\text{K}$ , and characteristic is shown both with and without a microscope light shining on diode.

We have also measured the capacitance-voltage relation for these devices. The capacitance decreased with increasing reverse voltage as  $V^{-0.4}$ , suggesting that the diode had a slightly graded doping profile. The zero-bias capacitance of approximately 25 pF is about the value expected for a 15-mil-square device on a substrate with a carrier concentration of  $1.3 \times 10^{16}/\text{cm}^3$ .

The photovoltaic properties of these diodes at  $300^\circ\text{K}$  were evaluated by measuring their blackbody responsivity using a  $700^\circ\text{K}$  blackbody and a 500-Hz chopping frequency, their relative spectral response using a prism spectrometer, and their noise using a PAR 112 preamplifier and a HP 302A wave analyzer. The measured noise voltage, 55 nV in a 1-Hz bandwidth, corresponds to the thermal noise in the diode resistance. The resulting curve of detectivity as a function of wavelength is shown for crystal A in Fig. I-5 where the detectivity increases with increasing wavelength from the visible, reaching a peak at  $1.7\ \mu$ . The peak detectivity for this diode was  $2.2 \times 10^{11}\ \text{cm}\sqrt{\text{Hz}}/\text{W}$ , and the quantum efficiency was about 15 percent at  $1.7\ \mu$ . For



Fig. I-5. Detectivity vs wavelength for three photovoltaic detectors fabricated in  $\text{Hg}_{1-x}\text{Cd}_x\text{Te}$ . A  $2\pi$ ,  $300^\circ\text{K}$  background was used for these measurements, and each device was  $15 \times 15$  mil square. Diode operating temperatures and peak quantum efficiencies are shown in figure. For diode A:  $x = 0.50$ , and diode zero-bias resistance and capacitance were 200 kohms and 25 pF, respectively; for B:  $x = 0.31$ , resistance = 3 megohms, and capacitance = 80 pF; for C:  $x = 0.25$ , resistance = 1 kohm, and capacitance = 120 pF.



wavelengths shorter than  $1.7 \mu$ , the response decreases more rapidly than would be expected for a quantum detector, suggesting that there is substantial surface recombination or recombination in the n-type layer of these devices. The cutoff wavelength of this detector ( $\sim 2 \mu$ ) is in good agreement with the room-temperature bandgap of 0.6 eV for crystal A.

The experiments carried out on crystals B and C were similar to those done on crystal A except that, because of the smaller bandgaps for these samples, the electrical evaluations were done at  $77^\circ\text{K}$ . The bombardments are given in Table I-2. As expected, type conversion was observed in the bombarded layers, and diode characteristics were seen between the bombarded squares and the substrate. The photovoltaic properties of these devices were evaluated using the same procedure as for sample A, except that the blackbody temperature was  $500^\circ\text{K}$  because of the longer wavelength response of these diodes. The resulting curves of detectivity as a function of wavelength for samples B and C are also shown in Fig. I-5. Of particular interest are the results for sample B for which we have made several diodes with zero-bias resistances as large as 3 megohms at  $77^\circ\text{K}$ . The quantum efficiencies of these devices, measured using the short-circuit photocurrent response to the  $500^\circ\text{K}$  blackbody, was about 29 percent at  $3.8 \mu$ . The measured detectivity is close to the background-limited value for a detector with this quantum efficiency. We therefore repeated the detectivity measurements with an  $f/6$  shield, cooled to  $77^\circ\text{K}$  in front of the diode. The detectivity under these conditions was about three times larger than for the  $2\pi$ ,  $300^\circ\text{K}$  background, indicating that the detector was indeed background-limited under the  $2\pi$ ,  $300^\circ\text{K}$  conditions.

The response speed for diodes from sample B was measured by placing a diode in a 50-ohm coaxial system, and loading it with 50 ohms. The measured photocurrent response to a pulsed GaAs laser indicated that the rise and fall times for the detector were less than 15 nsec.

In summary, we have shown that it is possible to create n-type regions on p-type  $\text{Hg}_{1-x}\text{Cd}_x\text{Te}$  in the composition range of 50- to 25-percent CdTe, and to fabricate high-quality



## Section I

photovoltaic detectors using a technique of proton bombardment. In this process, the sample temperature never exceeds 60°C, considerably below that necessary for diffusion. The resultant detectors show high detectivities, good quantum efficiencies, and fast response speed. This method appears to hold considerable promise for fabricating photovoltaic detectors in  $\text{Hg}_{1-x}\text{Cd}_x\text{Te}$ . There is every reason to expect that the process can be extended to wavelengths outside the 1.7- to 7- $\mu$  region investigated here and that it will be capable of producing detectors with tailored wavelengths throughout the IR spectral region.

A. G. Foyt  
T. C. Harman  
J. P. Donnelly

### D. TYPE CONVERSION AND n-p JUNCTION FORMATION IN PbTe PRODUCED BY PROTON BOMBARDMENT

We have previously reported that proton bombardment can be used to convert both p-type InSb and p-type  $\text{Hg}_{1-x}\text{Cd}_x\text{Te}$  to n-type and we have used this technique to fabricate high-detectivity photovoltaic diodes in these materials (see Refs. 11 and 12, and Sec. I-C above). In this section, we wish to report the use of this same technique to convert p-type PbTe into n-type material, and to present some initial results on PbTe photovoltaic diodes prepared by this method.

The PbTe used in these experiments was grown by the Bridgman technique and isothermally annealed in a Te-rich PbTe atmosphere at 600°C for one week. A typical sample had a 77°K carrier concentration of  $7 \times 10^{18}/\text{cm}^3$  and a mobility of  $10,000 \text{ cm}^2/\text{V-sec}$ .

Initial experiments were carried out on the structure shown in Fig. I-6. After polishing, each sample was free-etched in HBr-5% Br for a few seconds and then electrolytic-etched until an undamaged pit-free surface was obtained. Using photolithographic techniques, thin ( $\sim 500 \text{ \AA}$ ) 5-mil Au contacts on 50-mil centers were then electroplated on the front surface of each

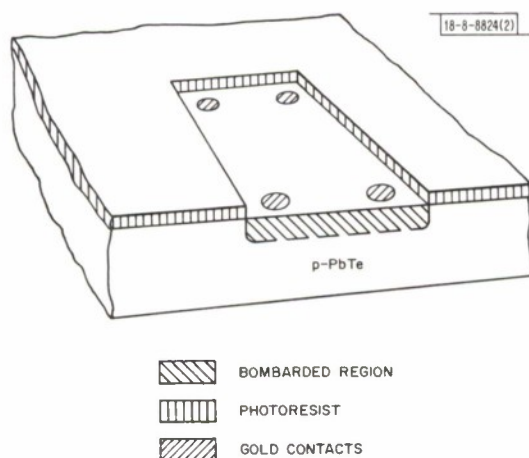


Fig. I-6. PbTe proton bombarded sample for Hall-van der Pauw measurements.

sample. These Au contacts were sufficiently thin that they had negligible stopping effect on the protons during subsequent bombardment. A thick layer of photoresist was then added to each sample and 65-mil-square holes opened in the photoresist as depicted in Fig. I-6. This photoresist layer is sufficiently thick to completely stop the protons used in these experiments. Therefore, only those areas from which the photoresist was removed were bombarded. Bombardment was carried out using a monoenergetic beam of 200-keV protons at a beam current density of approximately  $0.2 \mu\text{A}/\text{cm}^2$  for 500 sec, giving a total dose of  $5 \times 10^{14}$  protons/ $\text{cm}^2$ .

Following bombardment, various electrical measurements were carried out to evaluate the results. Thermoelectric probe measurements with

the sample at 77°K indicated that the bombarded areas had been converted to n-type material while the unbombarded areas remained p-type. Hall measurements of the van der Pauw type<sup>10</sup> performed using the four contacts in each square also indicated that the bombarded squares

were converted to n-type with a 77°K carrier concentration of approximately  $2 \times 10^{18}/\text{cm}^3$  and a mobility of  $12,900 \text{ cm}^2/\text{V-sec}$ , while the unbombarded squares remained p-type. Due to current leakage to the substrate in the van der Pauw measurements, the actual n-type carrier concentration obtained is probably considerably in error. Current-voltage measurements between various contacts were also performed at 77°K. Between two contacts on an unbombarded square, linear current-voltage characteristics with a resistance of 10 ohms were observed. Between two contacts on a bombarded square, linear current-voltage behavior was also observed, while diode characteristics were observed between a contact on the bombarded square and one on an unbombarded square or on the substrate. The diode characteristics were leaky, however, with zero-bias resistance of only a few hundred ohms. Nevertheless, by reducing the bombarded area to a 5-mil-diameter circle, zero-bias resistances over 1 megohm were observed.

Initial photovoltaic detectors were therefore fabricated as 5-mil diodes, as shown in Fig. I-7. After etching,  $1000 \text{ \AA}$  of  $\text{SiO}_2$  were deposited on the front face of each sample at  $340^\circ\text{C}$  using a silane-oxygen reaction (experiment has shown that this deposition of  $\text{SiO}_2$  has negligible effect on the carrier concentration and mobility of the substrate). A broad area Au ohmic contact was then electroplated on the back of each sample. By using photolithographic techniques, 3-mil holes on 10-mil centers were opened in the  $\text{SiO}_2$  and thin ( $\sim 500 \text{ \AA}$ ) Au contacts were electroplated in these openings. A thick layer of photoresist was then applied to the front surface and 5-mil holes concentric with the 3-mil contacts were opened in the photoresist as shown in Fig. I-7. The samples were then bombarded as previously described. Initial electrical measurements showed that the bombarded areas exhibited good diode characteristics to the back ohmic contact, while unbombarded areas were ohmic with a resistance of approximately 10 ohms. A typical 77°K current-voltage characteristic of a bombarded diode is shown in Fig. I-8. Also shown is the current-voltage characteristic with a microscope light shining on the diode. Zero-bias resistances in the dark as high as 2 megohms have been observed.

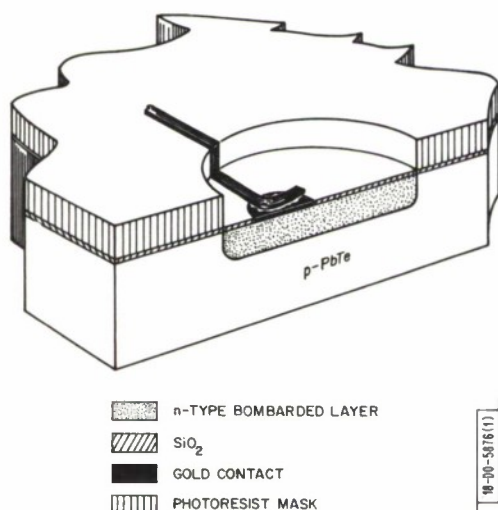


Fig. I-7. PbTe diode structure.

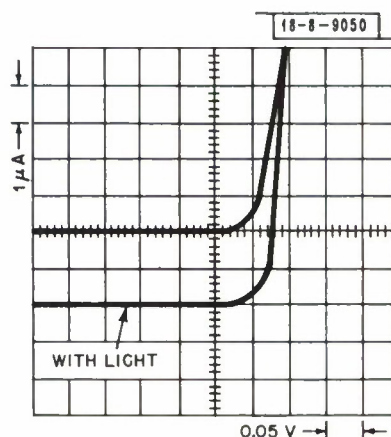


Fig. I-8. Current-voltage characteristics at 77°K of PbTe n-p junction photovoltaic detector.

## Section I

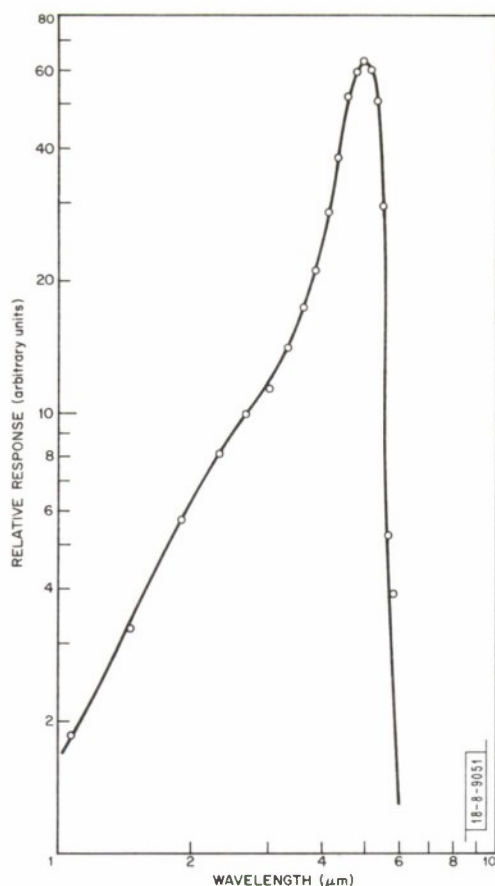


Fig. 1-9. Relative response of PbTe photovoltaic detector.

In order to study the photovoltaic properties of these diodes, they were mounted on TO5 headers. To accomplish this, additional Au followed by In was plated at room temperature on both the back and front contacts. The sample was then pressure-bonded to an In-plated TO5 header and a 1-mil Au wire pressed into the In on the 3-mil top contact.

Blackbody detectivity and relative response measurements were then carried out with the diode at 77°K. A typical relative response curve is shown in Fig. 1-9. The peak of the response occurs at 5 μm. The blackbody detectivity was measured using a 500°K blackbody and a 500-Hz chopping frequency. The largest value measured for these diodes was  $D^* (500, 500, 1) = 2.1 \times 10^{10} \text{ cm}\sqrt{\text{Hz}}/\text{W}$ . This measurement, combined with the relative response, gives a peak detectivity of  $1.3 \times 10^{11} \text{ cm}\sqrt{\text{Hz}}/\text{W}$  and a peak quantum efficiency of 29 percent at 5 μm. This detectivity is very close to the  $2\pi$ , 300°K background-limited value for a photovoltaic detector with this quantum efficiency. Reduction of the background using a cooled f/6 aperture resulted in a factor of two reduction in noise and an increase in peak detectivity to  $2.6 \times 10^{11} \text{ cm}\sqrt{\text{Hz}}/\text{W}$ . Under these conditions, the noise voltage is consistent with the calculated Johnson noise for the device.

The response speed of these diodes was measured by placing them in a 50-ohm coaxial system and loading them with 50 ohms. The diode response to a pulsed GaAs diode laser indicated that the rise and fall times are about 25 nsec. Since the diode capacitance is about 270 pF, it appears that these rise and fall times are due to RC limitations.

Although these results are only preliminary, they do indicate that proton bombardment may be a convenient method of making high-detectivity PbTe photovoltaic diodes. It will be interesting to determine if this same technique can be used to fabricate diodes in  $\text{Pb}_{1-x}\text{Sn}_x\text{Te}$ .

J. P. Donnelly  
T. C. Harman  
A. G. Foyt

## E. A LOW-POWER DENSITY GaAs/LiNbO<sub>3</sub> SURFACE WAVE AMPLIFIER

The semiconducting material used in a separated medium acoustic surface wave amplifier must have a low sheet carrier concentration  $n_s \sim 10^{10}/\text{cm}^2$  and a reasonably high mobility  $\mu \sim 1000 \text{ cm}^2/\text{V}\cdot\text{sec}$ . Although GaAs crystals can be obtained which appear capable of satisfying these requirements, there is a severe problem associated with the surface properties of this material. Surface treatments on GaAs tend to leave the Fermi level pinned at about 0.9 eV



below the conduction band.<sup>13</sup> Consequently, high-purity GaAs with  $n = 10^{13}/\text{cm}^3$  has a surface layer about  $10\text{ }\mu\text{m}$  deep which is depleted of carriers. Very little interaction between the mobile carriers and the surface waves on an adjacent piezoelectric can take place as the piezoelectric field of the wave does not penetrate this deeply at frequencies of interest  $\gtrsim 100\text{ MHz}$ .

Oxygen-compensated GaAs can be grown with the required low room-temperature carrier concentrations and, in addition, has a much larger concentration of deep donor levels.<sup>14</sup> The presence of these deep levels results in a considerable reduction of the depletion depth. Zero-bias Schottky barrier capacitance measurements on material with  $n \sim 5 \times 10^{12}/\text{cm}^3$  at room temperature show a depletion layer of less than  $1.5\text{ }\mu\text{m}$ , which is the depletion depth expected for a carrier concentration two orders of magnitude larger.

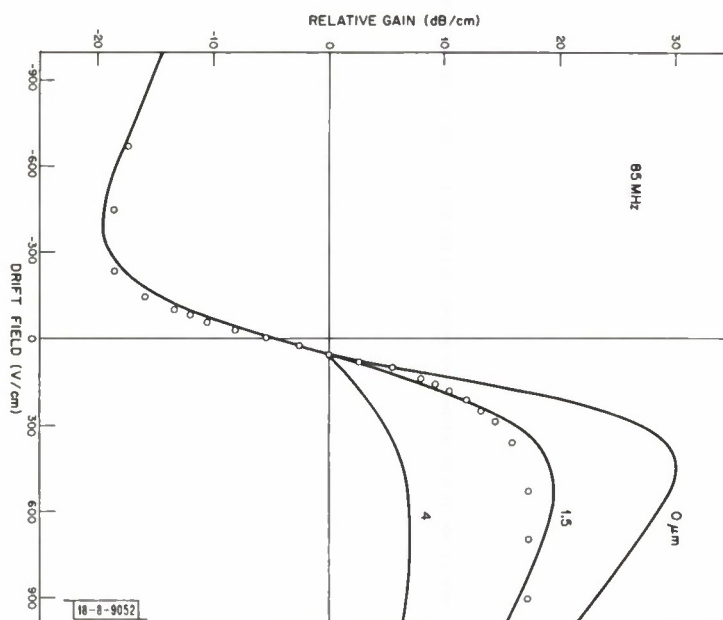


Fig. I-10. Experimental gain vs drift field data and theoretical curves for three different depletion depths.

Amplifiers made of this material show promising results. Figure I-10 presents the gain vs drift field characteristics of one of our first amplifiers. Theoretical curves are also shown for depletion layers of 0, 1.5, and  $4\text{ }\mu\text{m}$ , assuming  $n = 8 \times 10^{12}/\text{cm}^3$  and  $\mu = 6000\text{ cm}^2/\text{V-sec}$ . Both the low field slope  $\sim 0.08\text{ dB/V}$  and the maximum change in gain with field agree with the calculated values, indicating that the amplification is not significantly affected by the presence of the deep donor levels. The measured gain curve does show some asymmetry not present in the calculated curve, which may be due to trapping at these deep levels, or it may be a result of inhomogeneities in the crystal. The resistivity of this particular sample was found to vary from 100 to 200 ohm-cm over its 9-mm length. A more uniform 70-ohm-cm sample did not exhibit as much asymmetry.



## Section I

Although the peak gain here is only about one-half that expected for undepleted material, it still yields a relatively low-power dissipation factor. The optimum operating point is  $\sim 300$  V/cm where an electronic gain of 10 dB/cm is obtained. By polishing the crystal down to a thickness of 1 mil, this gain should be attainable with less than 100 mW/cm of DC power. The expected power dissipation figure of over 100 dB/W is much better than any previously reported in Si.<sup>15</sup>

D. L. Spears  
B. E. Burke

## F. CONDUCTIVITY STUDIES IN EUROPIUM OXIDE

The following is the abstract of a thesis submitted to the Department of Electrical Engineering, M.I.T., on 4 June 1970 in partial fulfillment of the requirements for the degree of Doctor of Science.

"The electrical and optical properties of EuO are studied in order to help determine conduction mechanisms. The resistivity of lightly doped material exhibits large changes with temperature and magnetic field, similar to that observed in the other Eu chalcogenides.

"A strong relationship is shown to exist between the electrical behavior of EuO and the parameters of the crystal growth process. EuO is grown by heating Eu metal and  $\text{Eu}_2\text{O}_3$  in a sealed tungsten crucible above the melting point of EuO and then cooling the mixture slowly. The ratio of Eu to O in the starting materials, the amount of dopant, if any, and the cooling rate all influence the electrical behavior of the product crystal. Two types of electrical behavior are observed, one having a peak in the resistivity vs temperature curve near the Curie point, the other not. The study of the first type of behavior forms the bulk of the thesis.

"The temperature dependence of the resistivity is a strong function of the doping level. In high-resistivity material, an activation energy behavior is observed above 200°K. For moderate resistivity material, an elbow in the resistivity is observed at 50°K, above which point the resistivity rises several orders of magnitude to a broad peak between 75° and 80°K. Above this peak, the resistivity levels off and varies little with temperature. In fairly heavily doped material the peak at 80°K becomes smaller and is shifted upward in temperature, following a similar shift in the Curie point.

"Optical absorption measurements show free-carrier-like absorption in moderately doped material. The absorption follows a  $\lambda^2$  law from  $2.2\mu$  out to  $10\mu$ , and continuously increases to at least  $20\mu$ . This result indicates that the conduction electrons are in a band at least 0.5 eV wide. Analysis of these results in terms of a free-carrier model yields an experimental value for  $n_c/\tau$ , where  $n_c$  is the carrier density and  $\tau$  is the scattering time. By combining this with conductivity results, both the

carrier density and scattering time can be determined as functions of temperature. Such an analysis shows that the large change in resistivity near the elbow at 50°K is primarily caused by carrier density changes and not mobility changes.

"This result and the temperature dependence of the resistivity in moderately doped material lead to a model of a trap level fixed in energy and a conduction band that varies in energy with temperature as does the optical absorption edge. The trap level is placed in energy to cross the conduction band edge at 50°K. By varying the ratio of electrons to traps about unity in the model, the wide range of observed resistivity behavior in EuO can be duplicated. Magnetoresistance and pressure data are also consistent with the model. The trap level is tentatively identified as an oxygen vacancy from crystal growth and annealing results.

"A model for the Curie point shift in heavily doped ferromagnetic semiconductors is presented. The Curie point change is predicted to vary as  $n_c^{1/3}$ . When reasonable parameters for EuO are used, good agreement with experiment is obtained."

M. R. Oliver

#### REFERENCES

1. T.C. Harman, Physics and Chemistry of II-VI Compounds, M. Aven and J.S. Prener, eds. (North-Holland Publishing Co., Amsterdam, 1967), p. 784.
2. B.E. Bartlett, J. Deans and P.C. Ellen, *J. Mats. Sci.* **4**, 266 (1969).
3. L.N. Swink and M.J. Brau, *Metallurgical Trans.* **1**, 629 (1970).
4. W.G. Pfann, *Trans. AIME* **203**, 961 (1955).
5. G.S. Cole and W.C. Winegard, *J. Inst. Metals* **93**, 153 (1964-5).
6. D. Long, *Phys. Rev.* **176**, 923 (1968).
7. C. Verie and J. Ayas, *Appl. Phys. Letters* **10**, 241 (1967).
8. W. Scott, 1970 Solid State Sensors Symposium, Conference Record (extended abstracts) (1970), p. 75.
9. E.N. Figurovskii, P.S. Kireev, A.V. Vanyukov, Yu. V. Evseev and A.P. Korovin, *Sov. Phys. - Semicond.* **3**, 1572 (1970).
10. L.J. van der Pauw, *Philips Res. Rept.* **13**, 1 (1958).
11. Solid State Research Report, Lincoln Laboratory, M.I.T. (1969:4), p. 3, DDC AD-701022.
12. *Ibid.* (1970:2), p. 6.
13. I. Flinn, *Surface Sci.* **10**, 32 (1968).
14. R.R. Senechal and J. Basinski, *J. Appl. Phys.* **39**, 4581 (1968).
15. K.M. Lakin, J.H. Collins and P.J. Hagon, *Proc. IEEE* **57**, 740 (1969).

## II. MATERIALS RESEARCH

### A. MELTING POINT MEASUREMENTS IN THE TRI-ARC FURNACE

A simple technique has been devised for utilizing the tri-arc furnace<sup>1,2</sup> in measuring the melting points of refractory materials. In this furnace, which was initially developed for crystal growth by the Czochralski method, samples can be rapidly melted under an argon atmosphere on a water-cooled copper or graphite hearth by means of three independently controlled DC arcs. The furnace offers several advantages for melting point measurements, including operation without a crucible and without contamination at temperatures up to at least 3500°C, and excellent visibility of the freezing interface.

The apparatus is shown schematically in Fig. II-1. A double-bore alumina thermocouple protection tube entering through an O-ring seal at the top of the furnace has been substituted for the seed holder used in crystal growth. No other modification of the equipment is necessary. Tungsten and tungsten-26% rhenium thermocouple wires 0.75 mm in diameter are inserted into the furnace through the alumina tube. To load the sample, the hearth is removed and replaced through the bottom of the furnace. The sample and thermocouple wires are easily observed at all temperatures through a Pyrex ring.

To make the measurements, the sample is first melted by means of one or two of the arcs, depending on the temperature required. The bare thermocouple wires are then lowered into the melt to a depth of about 2 mm. For conducting samples, the thermocouple circuit is completed

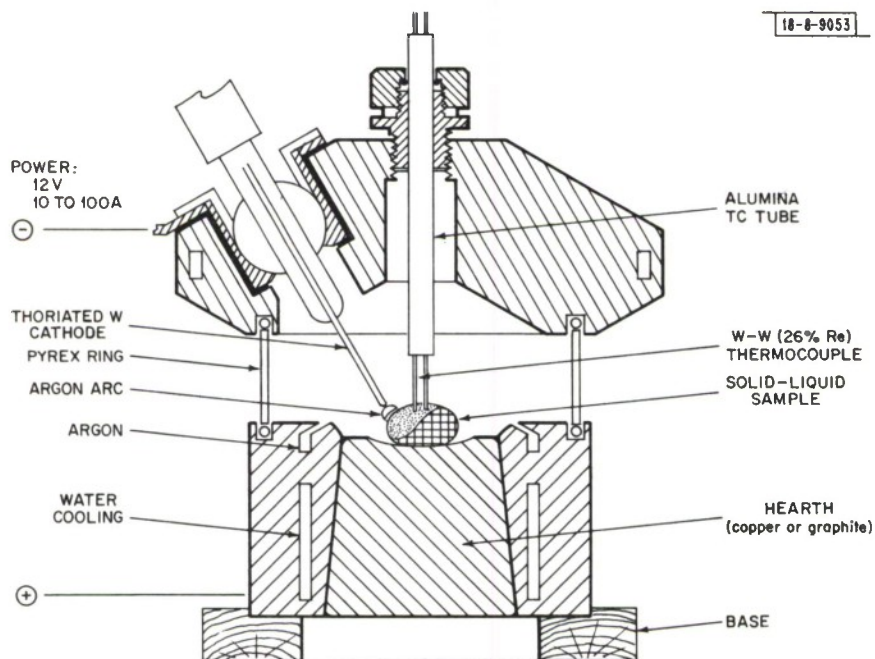


Fig. II-1. Apparatus for melting point measurements in tri-arc furnace.

## Section II

TABLE II-1  
MELTING POINT MEASUREMENTS WITH THE TRI-ARC FURNACE

	Melting Point (°C)		$T_m - T_a$ (°C)
	Measured ( $T_m$ )	Accepted ( $T_a$ )	
Ge	955 ± 20	937	+ 18
Au	1060 ± 5	1063	-3
Cu	1069 ± 5	1084	-15
Si	1412 ± 12	1410	+2
Ni	1460 ± 10	1452	+8
Pt	1780 ± 10	1770	+10
Ti	1610 ± 10	1667	-57
Th	1665 ± 10	1695	-30
Zr	1630 ± 20	1852	-222
TiO <sub>1.0</sub>	1680 ± 15	1750	-70
Ti <sub>2</sub> O <sub>3</sub>	1720 ± 35	—	—
VO <sub>1.26</sub>	1820 ± 30	—	—
NbO	1880 ± 15	1945	-65
FeO	1340 ± 10	1400	-60
Al <sub>2</sub> O <sub>3</sub>	2120 ± 35	2055	+65



through the melt; for insulating melts, an arc is used to weld the thermocouple wires into a bead before immersion. The sample is then cooled through the melting point by reducing the power to the arc(s), and the thermocouple voltage is monitored on a strip-chart recorder to determine the temperature during solidification.

To test the method, melting point measurements were made on the 15 elements and compounds listed in Table II-1. The samples weighed about 10 g each. In most cases, the melting point could be determined by thermal analysis, since thermal arrests of 7 to 20 sec were observed during freezing. The cooling rates ranged from about 3° to 10°C/sec, which was slow enough to permit convenient observation of the freezing interface as it moved across the sample. For a few materials, a definite thermal arrest was not observed. In these cases, the power was adjusted until the liquid-solid interface became stationary near the tip of the thermocouple, and the temperature recorded under these conditions was taken to be the melting point. Whether or not the material surrounding the thermocouple remained molten was indicated by the stability of the thermocouple signal, since convection in the liquid caused fluctuations in the signal which disappeared when the sample solidified. In several cases, the thermocouple wires were partially dissolved by the molten sample, but the amount dissolved was small enough, compared with the weight of the sample, that the melting point probably did not change appreciably. No measurements could be made on Fe, Co, or Nb because the thermocouple wires dissolved too rapidly.

Five independent melting point determinations, requiring a total of only about 15 minutes, were made for each sample. The average values are listed in Table II-1, together with accepted melting points (if available) and the differences between them. The reproducibility of the measurements (5° to 35°C) and the degree of agreement (2° to 18°C) with well-established values for six of the elements indicates that the values obtained by the present method are accurate to  $\pm 20^\circ\text{C}$ . Although considerably larger discrepancies are observed for Ti, Th, and Zr, these elements all tend to react with crucibles and dissolve oxygen, so that it is quite possible that the errors (particularly for Zr) are in the accepted values.

Both the reproducibility of the measurements and the agreement with accepted values are worse for the five oxides than for the elements. The variation in the results for  $\text{FeO}_x$  and  $\text{TiO}_x$  may be due in part to changes in sample composition, since these materials exist over a wide range of compositions. The greater disagreement with accepted values may reflect the fact that the melting points for the compounds are not as well established as those for the elements.

T. B. Reed

## B. CARRIER CONCENTRATION AND MOBILITY IN n- AND p-TYPE ZnTe:Al

Due to the presence of native acceptor defects associated with deviations from stoichiometry, undoped ZnTe is always p-type, whereas most other wide band gap semiconductors are n-type. We have determined the equilibrium carrier concentrations at 450° to 1000°C in ZnTe single crystals heavily doped with a donor (Al), and have observed both low resistivity n- and p-type behavior at compositions close to zinc or tellurium saturation, respectively.

Some of the crystals used had been grown<sup>3</sup> by the temperature gradient solution zoning method from a Te-rich solution. Others were obtained by an open-tube vapor transport method

## Section II

in which Pd-diffused  $H_2$  was used as the carrier gas to transport vapors of the pure elements to the deposition zone. Specimens approximately  $7 \times 6 \times 1$  mm cut from these crystals were purified by solvent extraction in liquid  $Zn^4$  at  $1000^\circ C$  for 4 days. Doping with Al was carried out by diffusion from a solution of liquid Zn containing 2 at. % Al at  $950^\circ C$  for 35 days. Spectrophotometric analysis of test samples diffused in this manner showed the Al content to be about  $1.8 \times 10^{20} cm^{-3}$ . Essentially the same concentration was measured in a sample annealed almost twice as long under the same conditions, indicating that equilibrium had been reached in both cases.

Measurements of the Hall coefficient and resistivity as a function of temperature and Zn or  $Te_2$  partial pressure were made with the apparatus previously used for similar measurements on ZnSe (Ref. 5), CdSe (Ref. 6), and CdTe (Ref. 7). The partial pressures were established by controlling the temperature of a reservoir containing pure Zn or pure Te. At the highest sample temperatures, the samples reached equilibrium with the vapor in a few minutes. With decreasing temperature, the time required for equilibration increased, reaching as much as 2 hours at  $450^\circ$  to  $500^\circ C$ . This increase in equilibration time, together with the rapid increase in the resistivity of n-type samples, set a lower limit on the temperature at which equilibrium properties could be measured.

The samples were n-type for Zn pressures close to saturation, and p-type for  $Te_2$  pressures close to saturation. The electron concentrations at the Zn-rich limit of the homogeneity range of ZnTe were obtained by making a very short extrapolation of the isotherms of concentration vs Zn pressure to the Zn pressures over Zn-saturated ZnTe (Ref. 8). A similar procedure was used to find the hole concentrations at the Te-rich limit, using the  $Te_2$  pressures over Te-saturated ZnTe (Ref. 8). The carrier concentrations found in this manner are plotted as a function of reciprocal absolute temperature in Fig. II-2, together with similar data for undoped ZnTe. (The dashed lines in the figure represent schematically the closure of the concentration loop in the vicinity of the melting point.)

For Te-saturated ZnTe, the hole concentrations in Al-doped and undoped samples are quite similar, although the difference between them increases appreciably with decreasing temperature.

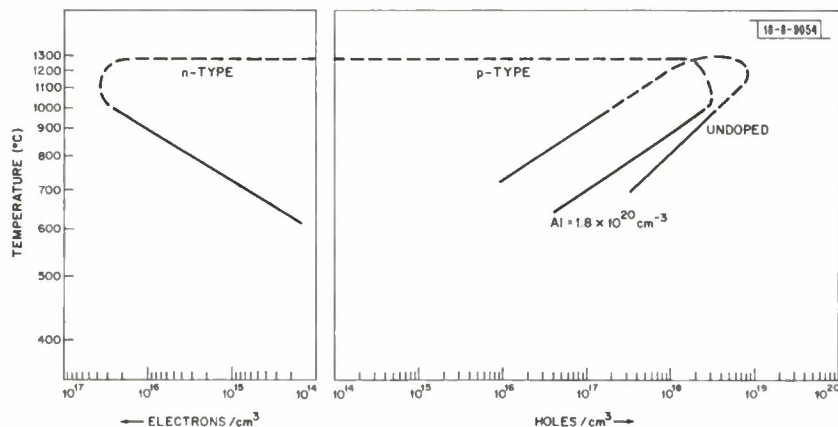


Fig. II-2. Carrier concentrations at Zn- and Te-rich limits of homogeneity range for undoped and Al-doped ZnTe.

In contrast, Zn-saturated samples are n-type, although the electron concentration is always far below the measured Al content. Even the maximum electron concentration is less than  $10^{17} \text{ cm}^{-3}$ , compared with the Al concentration of almost  $2 \times 10^{20} \text{ cm}^{-3}$ . The difference at  $950^\circ\text{C}$  cannot be explained by precipitation of Al, because it was introduced by diffusion under Zn-saturated conditions at this temperature. It is unlikely that precipitation of Al causes the reduction of electron concentration observed at lower temperatures, since the onset of precipitation would be expected to result in a change in the slope of the carrier concentration vs reciprocal temperature relationship. Other possible explanations include the presence of Al in some electrically inactive form (e.g., clusters), compensation by native acceptors, and association with a native defect to form an electrically inactive species. Evidence from paramagnetic resonance experiments for the formation of associates between Al atoms and single Zn vacancies has been obtained by Title, Mandel, and Morehead.<sup>9</sup>

With decreasing temperature, the resistivity of Al-doped, Zn-saturated ZnTe increases strongly. In an attempt to prepare n-type material with low resistivity at room temperature, several samples in sealed quartz ampoules were quenched in water at the completion of Al diffusion runs. The resistivities of these samples exceeded  $10^6 \text{ ohm-cm}$ . Since the ionization energy of the donors present has not been measured, it is not clear whether the high resistivities resulted because of incomplete quenching of the high-temperature defect concentration or because the donors are almost completely deionized at room temperature.

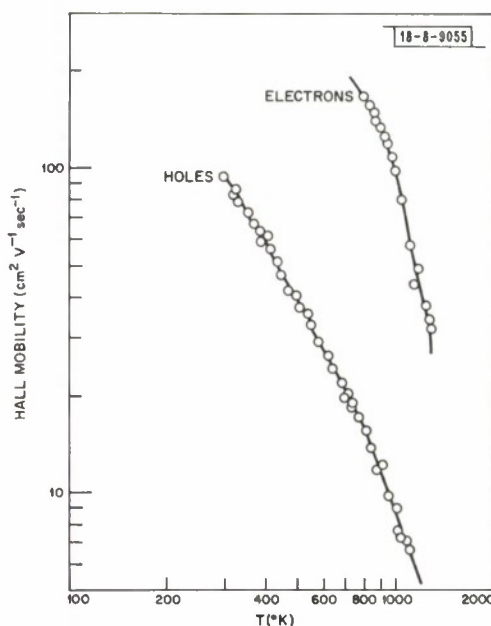


Fig. II-3. Hall mobilities of electrons and holes in ZnTe doped with  $1.8 \times 10^{20}$  Al atoms/cm<sup>3</sup>.

The Hall mobilities of electrons and holes measured in Al-doped ZnTe are plotted against temperature in Fig. II-3. At the highest temperatures, the mobility ratio  $b = \mu_e / \mu_h$  is about 11. If polar optical mode scattering is the dominant mechanism limiting the mobilities of both electrons and holes at these temperatures,  $b = (m_e^* / m_h^*)^{-3/2}$ . Adopting the value  $m_h^* = 0.6 m_0$  estimated<sup>10</sup> by analyzing the hole mobilities at low temperatures, this relationship yields  $m_e^* = 0.12 m_0$ .

F. T. J. Smith

## Section II

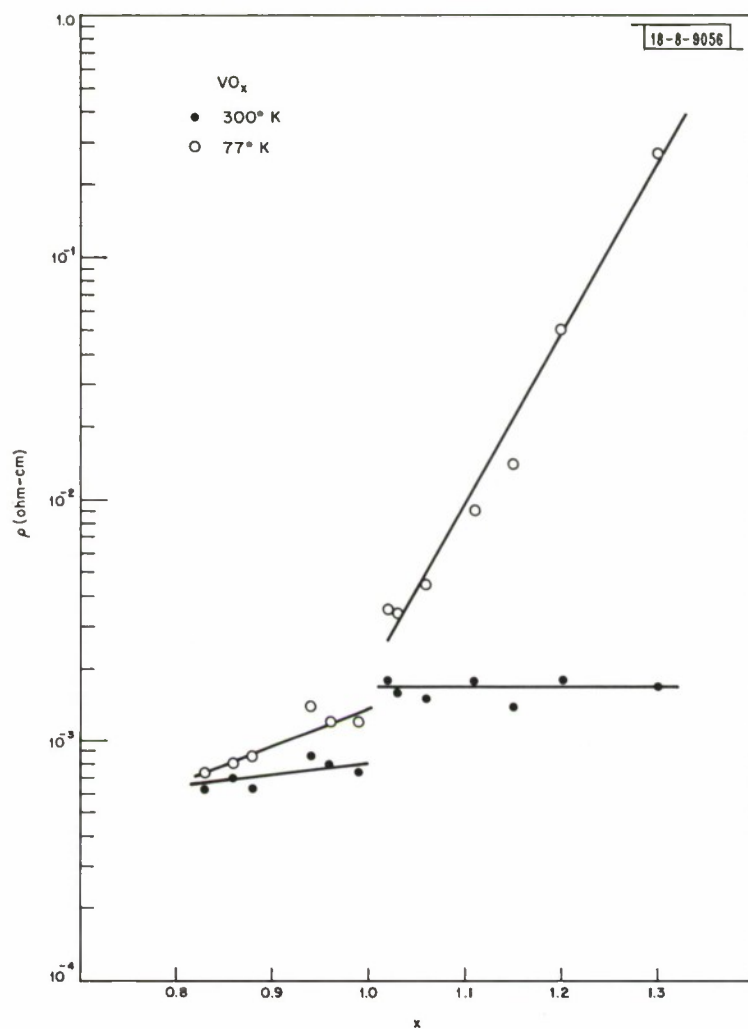


Fig. II-4. Resistivity ( $\rho$ ) at 77° and 300°K for VO<sub>x</sub> as a function of  $x$ .



### C. SEMICONDUCTING AND SEMIMETALLIC BEHAVIOR IN VO

Vanadium monoxide has an extremely wide homogeneity range, with  $x$  in  $\text{VO}_x$  ranging from 0.75 to 1.32. The compound has the defect rocksalt structure. As  $x$  increases from the V-rich stability limit to the O-rich limit, the percentage of V sites vacant increases from 11 to 22 percent, and the percentage of O sites vacant decreases from 31 to 0 percent. At the stoichiometric composition ( $x = 1$ ), 15 percent of the sites on each sublattice are vacant.

In a recent investigation of the structural, magnetic, and electrical properties of VO (Refs. 11, 12), we measured the electrical resistivity ( $\rho$ ) between 77° and 300°K for a series of samples spanning the homogeneity range. Contrary to some previous reports, no discontinuity in  $\rho$  as a function of temperature was observed in any case. The temperature coefficient of  $\rho$  was negative for all samples. For  $x < 1$ , the magnitude of the coefficient was small and almost independent of  $x$ ; but, for  $x > 1$ , it increased markedly with increasing  $x$ . These observations indicated that O-rich samples of VO are semiconductors, V-rich samples are semimetals, and the transition occurs at or very near the stoichiometric composition.

In order to obtain additional data concerning semiconducting and semimetallic behavior in VO, we have extended the measurements of  $\rho$  vs  $T$  to liquid helium temperature for five samples with  $x = 0.99, 1.11, 1.15, 1.20$ , and  $1.30$ . The sample with  $x = 1.30$  was cut from a single crystal grown by the Czochralski method in a tri-arc furnace and annealed in vacuum at 1300°C for 24 hours. The others were cut from polycrystalline rods cast in a chilled graphite mold and annealed in the same manner. The composition of each sample was determined by combustion analysis of a contiguous portion of the source ingot. Details of preparation and analysis are discussed in Ref. 12. Electrical contacts were made with silver-impregnated epoxy resin. The resistivity was measured by the DC van der Pauw technique at a series of fixed temperatures. Spot checks were made to be sure that the current-voltage relationship was linear at the sample currents used. Attempts to make Hall coefficient measurements at  $\sim 6$  kOe were unsuccessful because the Hall voltages were too low.

The results of the resistivity measurements are shown in Fig. II-4, where the values of  $\rho_{300}$  and  $\rho_{77}$  are plotted against  $x$ , and in Fig. II-5, where the ratio  $\rho/\rho_{300}$  is plotted against reciprocal absolute temperature. (Figure II-4 also includes values for a number of other samples with  $x \leq 1.06$ .) The data completely confirm our earlier results. No discontinuity in  $\rho$  vs  $T$  is observed over the entire temperature range for any sample. For the sample with  $x = 0.99$ ,  $\rho_{300} = 7.4 \times 10^{-4}$  ohm-cm at 300°K and increases by less than a factor of 2 down to 4.2°K. Even smaller changes in  $\rho$  over this range have been observed<sup>13</sup> in independent measurements on samples with  $x = 0.82, 0.83$ , and  $0.88$ . In contrast, for the samples with  $x > 1$ ,  $\rho$  increases by factors of  $10^3$  to  $10^9$  between 300°K and liquid helium temperature. For all of these O-rich samples,  $\rho_{300} = (1.6 \pm 0.2) \times 10^{-3}$  ohm-cm. (The values of  $\rho_{300}$  measured in earlier experiments<sup>12</sup> increased somewhat with increasing  $x$  for  $x > 1$ . These values are believed to be too high because electrical contact was made by ultrasonic soldering, which was later found to have introduced small cracks in some of the samples.) For the samples with  $x = 1.20$  and  $1.30$ , the maximum measured values of  $\rho$  are respectively  $4 \times 10^5$  ohm-cm at 4.2°K and  $1.3 \times 10^6$  ohm-cm at 8.3°K; measurements on the latter could not be extended to lower temperatures because the resistance became too high to be measured with our equipment.

## Section II

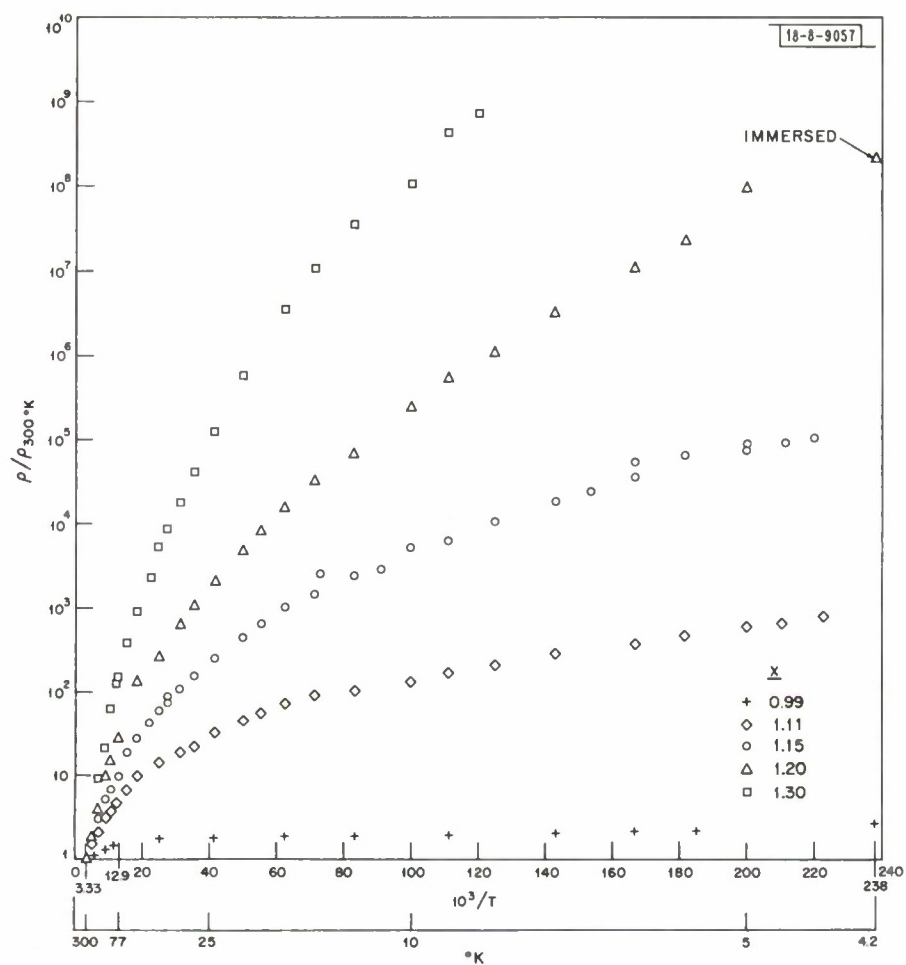


Fig. II-5. Ratio of resistivity to resistivity at 300°K ( $\rho/\rho_{300}$ ) vs  $10^3/T$  for five samples of  $VO_x$ .

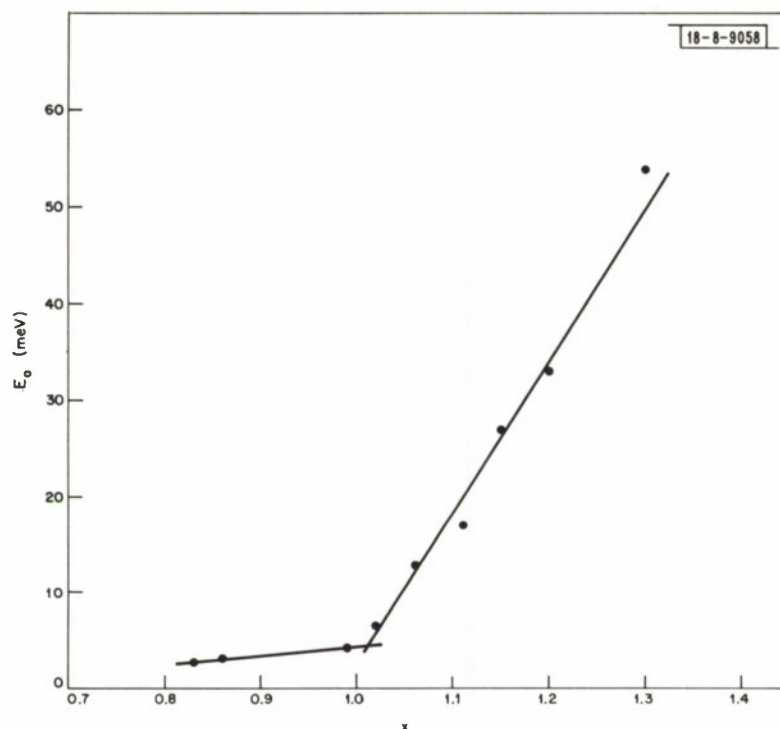


Fig. II-6. Activation energy ( $E_a$ ) vs  $x$  for  $\text{VO}_x$ .

Samples of VO with compositions near the O-rich stability limit are obviously semiconductors, since their low-temperature resistivities are far too high for them to be semimetals. It is less clear whether samples with V-rich compositions are semimetals or degenerate semiconductors, since either of these alternatives would be consistent with the essentially temperature-independent resistivity observed for these samples. We believe the former alternative is more likely, in view of the abrupt change in the composition dependence of the temperature coefficient of resistivity which occurs at  $x = 1$ . This change is shown in Fig. II-6, where activation energies ( $E_a$ ) obtained from the resistivity data are plotted against  $x$ . These values of  $E_a$  (which include a number obtained from earlier results<sup>12</sup> for  $x \leq 1.06$ ) were calculated from the slopes of the straight lines best fitting the data for  $\log \rho$  vs  $1/T$  between  $100^\circ$  and  $300^\circ\text{K}$ . A transition to semimetallic behavior at  $x = 1$  is also suggested by the changes observed<sup>12</sup> at that point in the sign of the Seebeck coefficient and in the slope of the molar susceptibility at  $4.2^\circ\text{K}$  as a function of  $x$ .

M. D. Banus  
T. B. Reed  
A. J. Strauss

#### D. CONCEPTUAL PHASE DIAGRAM AND ITS APPLICATION TO THE SPONTANEOUS MAGNETISM OF PYRITES

The compound  $\text{CoS}_2$  has the pyrite structure and is a ferromagnetic metal. Experimental studies of several pyrite systems having  $\text{CoS}_2$  as one end member have shown that these systems have complex magnetic properties and that they provide us an opportunity to study changes in magnetic properties as a function of changing bandwidth and band occupancy.

The one-electron energy diagram of Fig. II-7 has been constructed for  $\text{FeS}_2$  on the basis of symmetry arguments and empirical information, and, indeed,  $\text{FeS}_2$  and  $\text{FeSe}_2$  are known to be

## Section II

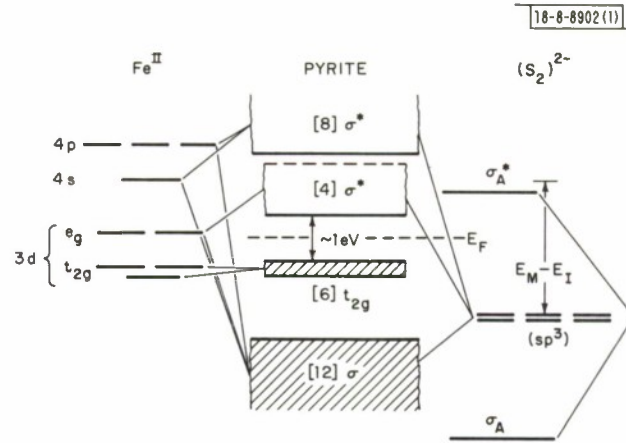


Fig. II-7. One-electron energy levels for outer electrons of  $\text{FeS}_2$  with pyrite structure.

diamagnetic semiconductors, the optical energy gap of  $\text{FeS}_2$  being about 0.9 eV. Since the narrow  $\sigma^*$  band is orbitally twofold-degenerate, this band should be one-quarter filled in  $\text{CoS}_2$  and half-filled in  $\text{NiS}_2$ . Furthermore, this is a cation sublattice d band, and the cations form a fcc subarray in the pyrite structure. Therefore, the narrow  $\sigma^*$  band cannot be split by the translational symmetry, and conventional band theory would predict  $\text{CoS}_2$  and  $\text{NiS}_2$  to be Pauli paramagnetic metals. The fact that  $\text{CoS}_2$  is a ferromagnetic metal and  $\text{NiS}_2$  is an antiferromagnetic semiconductor (in at least some preparations) therefore indicates that the  $\sigma^*$  band is too narrow for conventional theory to be applicable.

In order to interpret these results, it is useful to have a conceptual phase diagram as a function of three variables: the temperature  $T$  and band-occupancy number  $n_f$ , which are observable, and the near-neighbor transfer integral  $b$ , which is a measure of the strength of the interatomic interactions. The parameter  $b$  is not directly observable, but may be related qualitatively to the cation-anion covalent-mixing parameter  $\lambda_\sigma$ , since  $b \sim \lambda_\sigma^2$ . In conventional, tight-binding theory, the bandwidth is  $W_b \sim b$ . In localized-electron theory, the magnetic-ordering temperature due to superexchange coupling between near-neighbor-atom spins is proportional to  $b^2/U$ , where the electrostatic energy  $U$  decreases sharply with  $b$  in the transitional range of interatomic interactions  $b_c < b < b_g$  in which localized electrons are transformed into conventional itinerant electrons. Figures II-8 and II-9 show various phase diagrams that have been developed from physical arguments. An interesting feature for the quarter-filled band ( $n_f = 1/2$ ) is the transition from full-moment ferromagnetism  $F$  to a ferromagnetic spin-density wave  $FS$  to an antiferromagnetic spin density wave  $AFS$  to Pauli paramagnetism  $P_p$ , with increasing  $b$  as the overlap of occupied  $\alpha$ - and  $\beta$ -spin states increases from zero to equal occupation of  $\beta$ -spin states. According to this phase diagram, the ferromagnetic moment  $\mu_o = 0.84 \mu_B$  in metallic  $\text{CoS}_2$  indicates the presence of a  $FS$ , and the antiferromagnetic order in the more covalent  $\text{CoSe}_2$  (hence larger bandwidth  $W_b \sim b \sim \lambda_\sigma^2$ ) represents an  $AFS$  configuration.

In order to interpret the magnetic properties of mixed systems, it is necessary to reject a rigid-band model, since the energy separation between impurity bands and host bands is comparable to a bandwidth. Recognition that  $\text{Ni-S:S-Ni}\sigma^*$  bands are more stable than  $\text{Co-S:S-Co}\sigma^*$



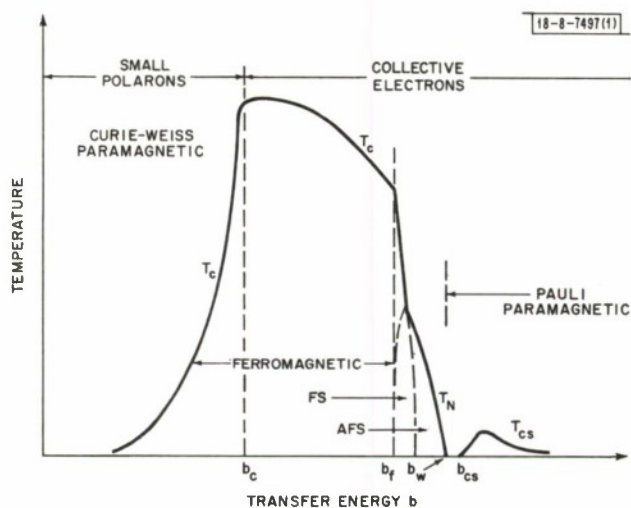


Fig. II-8. Temperature vs transfer energy diagram for  $n_l = 1/2, 3/2$ .

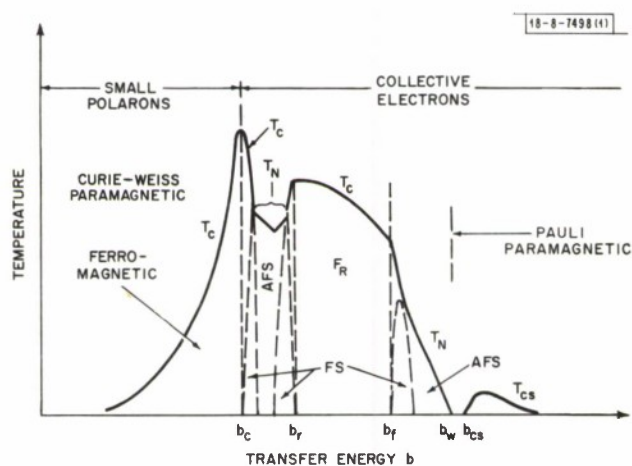


Fig. II-9. Temperature vs transfer energy diagram for  $n_l = 2/3, 4/3$ .

## Section II

bands, which are more stable than  $\text{Fe-S:S-Fe}\sigma^*$  bands, makes it possible to rationalize the maxima with  $x$  in the Curie temperature  $T_c$  and magnetization  $M_s$  in the system  $\text{Fe}_{1-x}\text{Co}_x\text{S}_2$  and the antiparallel coupling of substitutional  $\text{Ni}^{2+}$  ions. Similarly, recognition that  $\text{Co-S:Se-Co}$  and  $\text{Co-S:As-Co}\sigma^*$  bands have higher energy than  $\text{Co-S:S-Co}\sigma^*$  bands permits a consistent interpretation of the variations with composition in the Weiss constant  $\Theta_p$  and  $M_s$  in the systems  $\text{CoS}_{2-x}\text{Se}_x$  and  $\text{CoS}_{2-x}\text{As}_x$ .

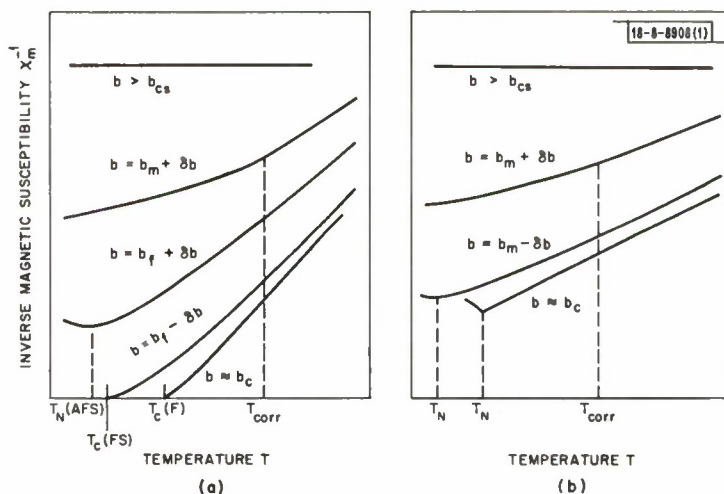


Fig. II-10. Inverse magnetic susceptibility vs temperature for various values of  $b = b_m \pm \Delta b$ : (a)  $n_l = 1/2$ ; (b)  $n_l = 1$ .

Figure II-10(a-b) shows how the  $\chi_m^{-1}$  vs  $T$  curves may be expected to vary with  $b$ . Since there is greater covalent mixing with a  $\text{Ni}^{2+}$  than a  $\text{Co}^{2+}$  ion, the fact that  $\text{NiSe}_2$  is without spontaneous magnetism and  $\text{NiS}_2$  apparently has a  $b \approx b_m$  is consistent with a FS in  $\text{CoS}_2$  and an AFS in  $\text{CoSe}_2$ . Furthermore, the extremely large  $|\Theta_p| \approx 40 T_N$  found in  $\text{NiS}_2$  as well as its  $\mu_{\text{Ni}} \approx 1.17 \mu_B < 2 \mu_B$  in this magnetically ordered phase vs a  $\mu_{\text{eff}} > 3.1 \mu_B$  in the paramagnetic state are consistent with  $b \approx b_m$  and Fig. II-10. They illustrate well the dangers associated with any attempts to interpret the paramagnetic-susceptibility data of itinerant-electron magnetism in terms of localized-electron concepts.

J. B. Goodenough

### E. VOLUME COMPRESSION MEASUREMENTS BY X-RAY DIFFRACTION STUDIES AT HIGH PRESSURES

The volume compression of materials with structures of high symmetry can be determined to pressures as high as 500 kbars by using x-ray diffraction techniques<sup>14</sup> to measure their lattice parameters as a function of pressure. The internal pressure on the sample is best found by simultaneously measuring the lattice parameter of a marker material intimately mixed with the sample. The pressure is then obtained from tabulated values of  $V/V_0$  vs  $P$  calculated from the equation of state for the marker. Reliable equations of state for several cubic materials, with coefficients calculated from the elastic constants measured at atmospheric pressure, have been derived from various theoretical models. Decker, *et al.*<sup>15</sup> have recently reviewed the calculations for NaCl, the most common marker material. Accurate lattice parameters can be obtained for

NaCl because six or seven lines of its fcc diffraction pattern can generally be observed with high-pressure equipment, and these parameters can be used to determine the pressure with considerable precision because the compressibility of NaCl is fairly large, particularly up to 100 kbars. Other marker materials include NaF, MgO, Al, and Ag which are useful when the NaCl lines interfere with those of the sample. In most cases, their compressibility has either been measured by shock methods or has been related to that of NaCl by x-ray diffraction measurements on mixtures with NaCl.

The accuracy of volume compression measurements made by the x-ray method obviously depends on the accuracy of the lattice parameter values determined for the sample and marker materials. The best diffraction patterns are obtained with diamond-anvil squeezers which use a curved film and with units employing electronic detection, in which data obtained by step-scanning the diffracted beam are converted by computer to intensity plots. Measurements in our laboratory are made with diamond-anvil units. We shall discuss several factors which affect the accuracy of lattice parameters obtained with this type of equipment, including the number and selection of the diffraction lines used, the sharpness of the lines, the constancy of the film-to-specimen distance, and the use of flat and curved films. The factors of film shrinkage and the change in absorption error due to changes in absorption and shape of the sample under pressure, which have been adequately treated by Jamieson,<sup>16</sup> will not be considered. The discussion will be illustrated primarily by experimental results which we have obtained for NaCl used as a marker, but it is equally applicable to measurements made on the sample material.

In general, the accuracy of the lattice parameter values increases with increasing number and sharpness of the diffraction lines. As a typical result of their measurements on a mixture of NaCl and Nb, Jamieson and Olinger<sup>17</sup> report  $a_0 = 5.152 \pm 0.0048 \text{ \AA}$  for the average lattice parameter of NaCl obtained from a diffraction pattern containing eight NaCl lines, where  $0.0048 \text{ \AA}$  is the standard deviation of the  $a_0$  values calculated for the individual lines. This result corresponds to a pressure of  $125.0 \pm 2.5$  kbars. In our experience, such high precision is obtained only if special care is taken to obtain a pattern containing at least seven or eight sharp lines. The more usual level of precision is represented by the value of  $a_0 = 5.372 \pm 0.028 \text{ \AA}$ , corresponding to  $49.5 \pm 7.5$  kbars, which we determined from a pattern containing six NaCl lines obtained in measurements on a mixture of NaCl and  $\text{TiO}_{1.25}$ . (Unfortunately, most research reports do not include any estimate of the accuracy of the marker lattice parameter or of the pressure values; nor do they give enough experimental details to permit making such an estimate.)

Some authors have reported internal pressures based on  $a_0$  values calculated from only a single NaCl diffraction line. This procedure can be expected to result in appreciable errors, as illustrated by the results given in Table II-2 for a series of measurements at pressures between 2.5 and 108 kbars on a mixture of NaCl and TiO. For each pressure, a value of  $a_0$  was calculated from the d-spacing of each of the five or six diffraction lines observed. The first and second columns of the table list the average of these individual  $a_0$  values and the corresponding pressure obtained from the tabulation of Decker, *et al.*<sup>15</sup> The other columns give the differences between the average  $a_0$  values and the individual values for the strong 200, 220, 222, and 400 lines, together with the corresponding pressure differences which are seen to be appreciable, but not at all systematic. Furthermore, additional experiments showed that, even at a given pressure, the relationship between the average and any individual  $a_0$  value changed appreciably



Average $a_a$ , All Lines <sup>‡</sup> (Å)	P <sup>§</sup> (kbars)	$\Delta a_a$ 200 (Å)	$\Delta P$ (kbars)	$\Delta a_a$ 220 (Å)	$\Delta P$ (kbars)	$\Delta a_a$ 222 (Å)	$\Delta P$ (kbars)	$\Delta a_a$ 400 (Å)	$\Delta P$ (kbars)
5.618	2.5	+0.002	-0.5	-0.008	+1.0	-0.003	+0.5	+0.031	-2.5
5.595	6.0	+0.005	-1.0	-0.004	+0.5	+0.001	-	+0.018	-3.0
5.589	7.0	+0.011	-1.5	-0.005	+0.5	-0.008	+1.0	+0.012	-1.5
5.555	12.0	-0.014	+1.5	-0.009	+1.0	+0.012	-1.5	+0.019	-2.0
5.541	13.5	-0.019	+2.0	+0.011	-1.5	+0.016	-1.5	+0.029	-3.0
5.523	17.0	-0.021	+4.0	+0.010	-2.0	+0.010	-2.0	+0.024	-4.5
5.506	20.0	-0.013	+2.5	-0.005	+1.0	+0.012	-2.0	-	-
5.456	29.5	-0.010	+2.5	-0.016	+4.0	+0.016	-4.0	-	-
5.302	69.0	-0.011	+3.0	+0.020	-6.0	+0.017	-5.0	-	-
5.190	108.0	-0.019	+8.5	+0.019	-8.5	+0.028	-12.5	-	-

<sup>‡</sup> The (111) lines were observed in all patterns and the (311) in most and are included in the average. However, they are not compared since they are too weak to use as individual reference lines.

<sup>§</sup> Based on data of Decker, *et al.*<sup>15</sup>

from run to run. Because of these random errors, the precision of the measured pressures is significantly improved by basing them on the average  $a_o$  values, and it increases as the number of lines increases.

The sharpness of the diffraction lines depends largely on two factors, absorption effects which vary with sample thickness and pressure gradients across the portion of the sample which intercepts the x-ray beam. Line broadening due to absorption effects is probably insignificant with the usual diamond-anvil squeezer, in which the samples are generally only 0.03 to 0.10 mm thick when under pressure, although it is encountered in high-pressure equipment where the incident x-ray beam is normal to the pressure axis. However, appreciable broadening can be produced by pressure gradients since, in general, diamond-anvil units have sharper gradients than the other types of high pressure x-ray apparatus. This broadening can be minimized by reducing the diameter of the incident x-ray beam to less than about 1/4 the diameter of the smaller diamond face, although this increases the required exposure time. For example, with a 0.020-inch-diameter moveable ("piston") diamond, decreasing the final collimator diameter from 0.010 to 0.005 inch greatly increases the sharpness of the diffracted lines but requires an increase in exposure time from ~60 to ~250 hours for satisfactory line densities with conventional x-ray sources. To attain pressures of 100 to 200 kbars it is necessary to use ~0.010-inch-diameter piston diamonds, ~0.002-inch-diameter collimators, and exposures of ~500 hours unless high-intensity micro-focus x-ray generators are employed.



Line broadening will also occur unless the internal pressure is kept constant throughout the exposure. This becomes more difficult with increasing exposure time. Pressure fluctuations will result from changes in loading, creep in the structures holding or loading the diamonds, and extrusion of the sample out of the high-pressure area. It is easiest to maintain pressure stability in gas-loaded equipment, provided that an adequate constant pressure regulator is used to maintain the loading, since gas supplied through the regulator will compensate for mechanical creep or sample extrusion. (Usually, extrusion is not a problem near room temperature, although it has been observed at room temperature for soft materials such as  $\text{Ag}_2\text{Te}$  and at 200° to 300°C for  $\text{InSb}$ .) In units mechanically loaded by a direct screw or screw-loaded spring, the internal pressure will be decreased by creep or yielding of the loaded structures. These problems must be eliminated by careful design and testing in order to obtain sharp patterns, particularly above 50 kbars.

Mechanical deformation can lead to significant errors in the measured values of  $a_0$  by changing the film-to-specimen distance  $R$ , which is used in calculating  $a_0$  from the positions of the diffraction lines on the film. This distance is determined by the relative positions of the film cassette and the seat and seat support for the fixed ("anvil") diamond. Under load, the table of the diamond punches into the seat, decreasing  $R$  from its initial value. Since this is a plastic deformation, errors due to this decrease can be avoided simply by measuring  $R$  after the diamonds have been loaded to the maximum in a preliminary squeeze. To make certain that  $R$  has not changed during a series of experiments, a diffraction pattern can be made at the conclusion of the series with the pressure completely released. At the end of one run with  $\text{TiO}$  and  $\text{NaCl}$  in a Bassett unit, for example, the diffraction pattern gave  $a_0$  values of  $4.177 \pm 0.005 \text{ \AA}$  for  $\text{TiO}_{1.0}$ , and  $5.625 \pm 0.003 \text{ \AA}$  for  $\text{NaCl}$ . This shows that  $R$  did not change significantly during the run.

The seat or seat support may also yield elastically, however. The change in  $R$  from this source may be determined in a blank run by using the measured value of  $R$  to determine  $a_0$  as a function of pressure for a wafer of  $\text{NaCl}$  glued to the back of the anvil diamond in the exit slot. Apparent changes in  $a_0$  will reflect changes in  $R$  due to the motion of the diamond. In some experiments of this type, at pressures up to 100 kbars no change in  $R$  could be detected, but in others, appreciable changes occurred. For example, in one unit with a 0.039-inch piston diamond face and a 0.010-inch collimator, the apparent  $a_0$  determined from six lines (including the 420) increased steadily from  $5.832 \text{ \AA}$  at 18 kbars to  $5.844 \text{ \AA}$  at 98 kbars. This indicates a decrease in  $R$  over this range of 0.126 mm out of approximately 50 mm, which would lead to an error of -4.5 kbar in the internal pressure determined at 100 kbars. (In principle, the compression of the anvil diamond under load will also result in a decrease in  $R$ , but this decrease is not significant because the compressibility of diamond is so small.)

Two types of film cassettes are generally used with diamond-anvil squeezers, one which is flat and perpendicular to the x-ray beam and the other which is curved to form a segment of the circumference of a circle. For both types, the value of  $R$  is determined by pressing an  $\text{NaCl}$  wafer between the piston and anvil diamonds to the maximum load anticipated and then relaxing the load completely. If the wafer sticks to the anvil diamond, as is usually the case, a diffraction pattern is taken. The value of  $R$  is chosen to yield the atmospheric pressure value of  $a_0$  for  $\text{NaCl}$  from the positions of the diffraction lines.

## Section II

The flat cassette is the simpler type to construct and position. One disadvantage is that in some cases the film does not remain flat against the back of the cassette. This bowing can be detected because it leads to a systematic change in the values of  $a_0$  as a function of diffraction line angle ( $2\theta$ ). Such a change is illustrated by the results labeled "film apparently bowed" in Table II-3, which were obtained for a diffraction pattern measured at  $\sim 4$  kbars. A systematic decrease in  $a_0$  with increasing hkl value is superimposed on the scatter due to random error, whereas there is no systematic change for the  $a_0$  values labeled "flat film." It is clear that, in order to distinguish the two cases, it is necessary to read all the diffraction lines, not just one or two.

TABLE II-3				
LATTICE PARAMETER MEASUREMENTS ON NaCl IN A GAS-LOADED DIAMOND-ANVIL UNIT				
hkl	Film Apparently Bowed		Flat Film	
	d	a	d	a
111	—	—	3.2385	5.609
200	2.8126	5.625	2.8122	5.624
220	1.9855	5.615	1.9838	5.610
222	1.6254	5.630	1.6199	5.611
400	1.4054	5.622	1.4019	5.608
420	1.2536	5.606	1.2556	5.615
422	1.1418	5.594	1.1470	5.619
	Average of 6, $a_a = 5.615$ (~4 kbars)		Average of 7, $a_o = 5.614$ (~4 kbars)	
The 311 and 331 lines were obscured by the other pattern.				

The curved cassette is much more difficult to align than the flat type, since the center of the circle must coincide with the sample. However, the curved cassette has the important advantage that the path length in air is the same for all diffraction lines, rather than increasing for the higher index, lower intensity lines as it does with the flat cassette. Therefore, it is possible to obtain lines at higher  $2\theta$  which cannot be observed with the flat cassette because of absorption by air. The best films obtained with curved cassettes give NaCl patterns with 12 lines up to the 442 ( $2\theta = 44.19^\circ$ ). In addition, the curvature forces the film against the back of the cassette and prevents bowing. If the cassette is correctly positioned, the  $a_0$  values obtained for the different lines will exhibit only random variations, not a systematic change with  $2\theta$ .

M. D. Banus  
Mary C. Lavine

## REFERENCES

1. T.B. Reed in High Temperature Technology (Butterworths, London, 1967), p. 655.
2. T.B. Reed and E. R. Pollard, J. Cryst. Growth 2, 243 (1968), DDC AD-681586.
3. J.M. Steininger, Materials Res. Bull. 3, 595 (1968), DDC AD-674790.
4. M. Aven and H.H. Woodbury, Appl. Phys. Letters 1, 53 (1962).
5. F.T.J. Smith, Solid State Commun. 7, 1757 (1969).
6. ———, Ibid. 8, 263 (1970), DDC AD-707495.
7. ———, Metallurgical Trans. 1, 617 (1970), DDC AD-707569.
8. R.F. Brebrick, J. Electrochem. Soc. 116, 1274 (1969), DDC AD-696239.
9. R.S. Title, G. Mandel and F. F. Morehead, Phys. Rev. 136, A300 (1964).
10. M. Aven and B. Segall, Phys. Rev. 130, 81 (1963).
11. Solid State Research Report, Lincoln Laboratory, M.I.T. (1969:2), p. 17, DDC AD-690997.
12. M.D. Banus and T.B. Reed in The Chemistry of Extended Defects in Non-Metallic Solids (North-Holland Publishing Co., Amsterdam, 1970), p. 488.
13. J.M. Honig, W. E. Wahnsiedler, M.D. Banus and T.B. Reed, J. Solid State Chem. 2, 74 (1970).
14. M.D. Banus, High Temperatures-High Pressures 1, 483 (1969).
15. D.L. Decker, W.A. Bassett, L. Merrill, H. T. Hall and J.D. Barnett, "High Pressure Calibration - A Critical Review," High Pressure Data Center, Brigham Young University (October 1969).
16. J.C. Jamieson, Metallurgy at High Pressures and High Temperatures, K.A. Gschneider, ed. (Gordon and Breach, New York, 1964), p. 201.
17. J.C. Jamieson and B. Olinger, International Conference on Accurate Characterization of the High Pressure Environment, National Bureau of Standards, Gaithersburg, Maryland, 14-18 October 1968.



### III. PHYSICS OF SOLIDS

#### A. ELECTRONIC BAND STRUCTURE

##### 1. Interband Magnetoreflexion of $\text{Hg}_{0.839}\text{Cd}_{0.161}\text{Te}^\dagger$

Interband oscillatory magnetoreflexion has been observed on a sample of  $\text{Hg}_{0.839}\text{Cd}_{0.161}\text{Te}$  which is homogeneous to within the error of the electron microprobe. This material was grown by the new method described in Sec. I-B. At 4.2°K, it has an electron concentration of  $9.4 \times 10^{14} \text{ cm}^{-3}$  and a Hall mobility of  $2.6 \times 10^6 \text{ cm}^2/\text{V-sec}$  which, so far as we know, is the highest mobility observed to date for  $\text{Hg}_{(1-x)}\text{Cd}_x\text{Te}$ . About twenty magneto-optical transitions have been seen in the photon energy range 0.05 to 0.30 eV. The overall quality of the magnetoreflexion is comparable to that of the best InSb and  $\alpha$ -Sn. Oscillatory amplitudes as high as 40 percent of the zero-field reflectivity have been observed.

The  $\Gamma_6$  to  $\Gamma_8$  energy separation for a material of this composition is expected to be very close to zero. A comparison of our data taken at  $\sim 30^\circ$  and  $\sim 90^\circ\text{K}$  shows that the transition energies and the reduced effective mass increase with temperature. Since the  $\Gamma_6$  energy increases with respect to the  $\Gamma_8$  energy with increasing temperature, in this composition region, these temperature effects show that  $E(\Gamma_6) > E(\Gamma_8)$ , at least at the higher temperature. We hope that by fitting theoretical and experimental energies we can determine the value of the small energy gap, which is much less than the lowest photon energy used, 0.05 eV.

The splitting between transitions from the  $(n-1)^{\text{th}}$  and  $(n+1)^{\text{th}}$  heavy hole levels to the  $n^{\text{th}}$  conduction band level is observed, and this gives a direct determination of the heavy hole mass. A preliminary value for this parameter is  $m^* = 0.2$  to  $0.3m$ . The value of the  $\vec{k} \cdot \vec{p}$  interaction parameter which has been used to fit intraband experiments,  $E_p = 17 \text{ eV}$ , gives a reasonable preliminary fit to our data.

The sample investigated has a (100) surface, which is perpendicular to the magnetic-field direction in our experiment. Such a configuration gives the simplest magnetoreflexion spectrum. In future work, we hope to use samples with (111) surfaces to search for the extra "warping" and "linear-k" induced transitions.

S. H. Groves  
T. C. Harman  
C. R. Pidgeon§

##### 2. Conduction Band Parameters for InSb

In the most recent determination of conduction band parameters for InSb, Johnson and Dickey<sup>1</sup> find that the band edge effective mass  $m^*$  and g-factor  $g^*$  cannot be entirely accounted for by the  $\vec{k} \cdot \vec{p}$  interaction between the conduction and valence bands. For example, with their value of mass  $m^* = 0.139m$ , determined from cyclotron resonance, a value  $g^* = -48$  is predicted

† This research was carried out using the facilities of the Francis Bitter National Magnet Laboratory, M.I.T.

§ Francis Bitter National Magnet Laboratory, M.I.T.



### Section III

using the conduction-valence band interaction expression of Roth<sup>2</sup> with the experimentally determined parameters  $E_g = 0.236 \text{ eV}$  and  $\Delta_v = 0.815 \text{ eV}$ , where  $E_g$  is the energy gap and  $\Delta_v$  is the spin-orbit splitting of the valence band at  $k = 0$ . However, the value found from the ESR measurements of Isaacson<sup>3</sup> is  $g^* = -51.3 \pm 0.1$ . Johnson and Dickey conclude that higher band interactions must be included to account for the values of  $m^*$  and/or  $g^*$ .

For diamond lattice materials, the only higher bands which have a  $\vec{k} \cdot \vec{p}$  interaction with the s-like conduction band have  $\Gamma_{25}$  symmetry, and these are thought to be too far removed to have the effect required. If the zincblende lattice, appropriate to InSb, is considered as a diamond lattice plus a perturbing antisymmetric potential, the bonding p-like valence band wave functions ( $\Gamma_{25}$ ) admix with the antibonding p-like conduction band wave functions ( $\Gamma_{15}$ ).<sup>4</sup> This alters the diamond lattice expression for the effective mass and g-factor, as discussed by Cardona.<sup>5</sup> The purpose of this section is to show that the admixing qualitatively accounts for the apparent discrepancy and that, with values of band parameters which are not unreasonable, the measured mass and g-factor values can be calculated from  $\vec{k} \cdot \vec{p}$  theory.

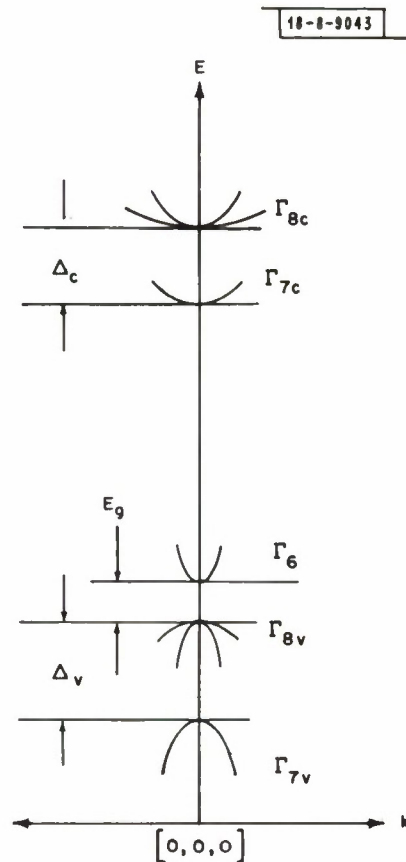


Fig. III-1. Bands at  $\vec{k} = 0$  for InSb which influence size of effective mass and g-factor of  $\Gamma_6$  conduction band.  $\Delta_c$  and  $\Delta_v$  are spin-orbit splittings, and  $E_g$  is energy gap.

Figure III-1 shows the bands of interest for our discussion. The  $\Gamma_{8c}$  and  $\Gamma_{7c}$  representations derive from the  $\Gamma_{15}$  single-group representation.  $\Delta_c$  is a spin-orbit splitting. The  $\Gamma_{8v}$  and  $\Gamma_{7v}$  representations derive from the diamond lattice, single-group representation  $\Gamma_{25}$ .

The  $\Gamma_6$  band is the lowest conduction band whose parameters we are discussing. The  $\Gamma_6$  band mass and g-factor in the absence of the antisymmetric potential are given by<sup>2</sup>:

$$m/m^* = 1 + \frac{E_p}{3} \left[ \frac{2}{E_g} + \frac{1}{(E_g + \Delta_v)} \right] \quad (\text{III-1})$$

$$g^*/g = 1 - \frac{E_p}{3} \left[ \frac{1}{E_g} - \frac{1}{(E_g + \Delta_v)} \right] \quad (\text{III-2})$$

where  $E_p \equiv 2mP^2/\hbar^2$ , and  $P \equiv (i\hbar/m) \langle S | p_x | X \rangle$  is a momentum matrix element between the single-group basis functions of the conduction and valence bands. If  $|X\rangle$ , transforming as  $yz$ , is a single-group basis function of the p-like valence band and  $|x\rangle$  is that of the p-like conduction band, the antisymmetric potential gives admixed wave functions  $a|X\rangle + b|x\rangle$  and  $a|x\rangle - b|X\rangle$  for the valence and conduction bands, respectively, where  $a$  and  $b$  are real coefficients.<sup>5</sup> In this situation, it can be shown that

$$m/m^* = 1 + \frac{E_p}{3} \left\{ a^2 \left[ \frac{2}{E_g} + \frac{1}{(E_g + \Delta_v)} \right] - b^2 \left[ \frac{2}{E(\Gamma_{8c})} + \frac{1}{E(\Gamma_{7c})} \right] \right\} \quad (\text{III-3})$$

$$g^*/g = 1 - \frac{E_p}{3} \left\{ a^2 \left[ \frac{1}{E_g} - \frac{1}{(E_g + \Delta_v)} \right] + b^2 \left[ \frac{1}{E(\Gamma_{8c})} - \frac{1}{E(\Gamma_{7c})} \right] \right\} \quad (\text{III-4})$$

where the zero of energy is taken at  $E(\Gamma_6)$ .

It is seen that the effect of the admixing is to reduce  $m/m^*$  and to increase the magnitude of  $g^*/g$ . Thus, if one ignores the admixing and uses the experimental value of  $m/m^*$  with Eq. (III-1) to determine  $E_p$ , and then uses the experimental value of  $g^*/g$  and Eq. (III-2) to do the same, the first value of  $E_p$  will be less than the second – which is another way of stating the observation of Johnson and Dickey.

To judge whether this idea is quantitatively reasonable, we use the experimental values of  $m/m^*$ ,  $g^*/g$ ,  $E_g$ ,  $\Delta_v$ , and values of  $E(\Gamma_{8c})$  and  $E(\Gamma_{7c})$  from OPW calculations.<sup>6</sup> This yields  $E_p = 30$  eV,  $a^2 = 0.81$ , and  $b^2 = 0.19$ . The quantities  $a$  and  $b$  can be expressed in terms of the separations between the upper and lower p-bands in InSb and in its isoelectronic diamond lattice partner  $\alpha$ -Sn (Ref. 5). This gives satisfactory agreement with the OPW results.<sup>7</sup> The value  $E_p = 30$  eV is in reasonable agreement with the value determined from intraband effective mass measurements<sup>8</sup> on  $\alpha$ -Sn ( $E_p = 28$  eV), but is considerably higher than the value determined from interband measurements<sup>9</sup> ( $E_p = 24$  eV). Effects such as these from the antisymmetric potential may also be observable in materials such as the  $\text{Hg}_{(1-x)}\text{Cd}_x\text{Te}$  alloys.

S. H. Groves

### 3. Polaron Self-Energy Effects in the Phonon-Assisted Cyclotron Resonance and the Second-Harmonic Cyclotron Resonance of InSb

We have observed polaron self-energy effects in the phonon-assisted cyclotron resonance and in the second-harmonic cyclotron resonance in InSb for photon energies near twice the known optical phonon energies of InSb. At these photon energies, and for appropriate magnetic fields,

### Section III

the unperturbed  $n = 0$  Landau level, two-optical phonon electron-lattice state; the  $n = 1$ , one-phonon state; and the  $n = 2$ , zero-phonon electron-lattice state converge. This convergence of the unperturbed electron-lattice states is a situation that is favorable for enhanced polaron self-energy effects. The background two-phonon lattice absorption is relatively weak and permits observation of the magnetically induced absorption throughout the energy region. This contrasts with the situation in the enhanced polaron self-energy experiment involving fundamental cyclotron resonance where observations are limited to the fringes of the energy region of interest.<sup>10</sup>

In the experiments, infrared absorption peaks are observed which have been attributed to transitions from the  $n = 0$  Landau level to (a) the  $n = 2$  Landau level and (b) the  $n = 1$  Landau level with the emission of an LO phonon. Companion absorption occurs involving impurity states which lie close to the respective Landau levels.<sup>11</sup>

In the present detailed examination of the magnetic field dependence of these absorption peaks, we observe discontinuities at characteristic energies of  $49.4 \pm 0.3$  and  $45.6 \pm 0.3$  meV. On the basis of a simple model, these energies would correspond to 2 LO and to 2 TO phonons, respectively. These energies compare favorably with values of  $24.4 \pm 0.3$  meV (2 LO =  $48.8 \pm 0.6$ ) and  $22.9 \pm 0.4$  meV (2 TO =  $45.8 \pm 0.8$ ) for LO and TO phonon energies observed in other experiments.<sup>11,12</sup> The agreement is quite good and indicates the existence of a significant electron-TO phonon interaction in a magnetic field in InSb. This conclusion is not affected by uncertainties in the magnitude of any electron energy level separations as was present in the experiments involving spin-flip cyclotron resonance.<sup>13,14</sup>

E. J. Johnson  
W. E. DeFeo

#### 4. Polaron Zeeman Effects in the Silver Halides<sup>†</sup>

Using a Grubb Parsons interferometer and a Bitter solenoid, we have measured the Zeeman splitting of a photo-induced, bound, p-state conduction electron in two strongly polar materials, AgBr ( $\alpha = 1.7$ ) and AgCl ( $\alpha = 2.0$ ) in magnetic fields up to 139 kG. In addition, we have measured the Zeeman splitting of the two most intense higher-frequency absorption bands in AgBr.

The splitting in the high magnetic fields of the  $168\text{-cm}^{-1}$  line in AgBr differs substantially from the predictions of the model<sup>15</sup> that successfully explains the low-field data. Specifically, the  $m = -1$  branch is pinned about 6 to  $6.5\text{-cm}^{-1}$  below the zero-field transition. This pinning is not due to the interaction between the 2p-state and the 1s-state plus one  $k = 0$  longitudinal optical phonon because the frequency involved is much larger than the optical LO phonon frequencies and the pinning is much weaker than that based on the Fröhlich Hamiltonian. The pinning may be due to the interaction of the 2p-state with the 1s-state plus one local mode phonon.<sup>16</sup>

The magnetic field splitting of the two prominent higher-frequency-induced absorption bands in AgBr at  $233$  and  $297\text{-cm}^{-1}$  differed substantially. The  $297\text{-cm}^{-1}$  band split in a similar but not quite identical manner to the  $168\text{-cm}^{-1}$  line. The lower branch of the  $297\text{-cm}^{-1}$  band did not appear to pin. However, the splittings are sufficiently similar to justify the identification of the  $297\text{-cm}^{-1}$  band as the one longitudinal optical phonon sideband of the  $168\text{-cm}^{-1}$  line. The  $233\text{-cm}^{-1}$  band did not split within our resolution of  $10\text{-cm}^{-1}$  for a line of its width. We have

---

<sup>†</sup> This research was carried out using the facilities of the Francis Bitter National Magnet Laboratory, M.I.T.



interpreted this effect on the basis of our model for the low-field data. This model predicted two 2p-states, one above and the other below the 1s-state plus one longitudinal optical phonon. When we adjusted our parameters so that the upper 2p-state had both the same energy and Zeeman mass as experiment, we found the lower 2p-state had an energy one longitudinal optical phonon below the  $233\text{-cm}^{-1}$  line and a Zeeman mass of  $3.5 \pm 0.5 m_e$ . The splitting of this state would only be  $3\text{cm}^{-1}$  at our highest fields. We therefore tentatively identify the  $233\text{-cm}^{-1}$  band as the one longitudinal optical phonon sideband of the lower 2p-state.

Induced infrared absorption in AgCl is both much smaller and more complex than in AgBr. Signal-to-noise problems and the complexity of the absorption made identification of the lines somewhat ambiguous. We tentatively determine a p-state Zeeman mass of  $0.75 \pm 0.10 m_e$ , 80 percent larger than the cyclotron mass<sup>17</sup> of  $0.42 m_e$ .

R. C. Brandt  
D. R. Cohn<sup>†</sup>

### 5. Laser Magnetospectroscopy in GaAs

Far infrared lasers (HCN, DCN, and  $\text{H}_2\text{O}$ ) have been used to study high-purity GaAs ( $n = 1.8 \times 10^{13}$ ) with resolution unattainable with conventional techniques. These measurements have revealed several new features in the absorption and photoconductivity spectra of the hydrogenic donors.

The observation that the  $1s \rightarrow 2p$  ( $m = +1$ ) transition actually consists of three lines is of particular interest. This splitting has been obtained at four different wavelengths and is believed to be a consequence of differing central cell shifts of the various donors. Interferometric studies<sup>18</sup> and mass spectrographic results<sup>19</sup> substantiate this identification in the high-purity material. In Fig. III-2, the photoconductivity and transmission of the epitaxial sample are plotted as a function of magnetic field for  $\lambda = 118\mu$  (water-vapor line). Only the  $1s \rightarrow 2p$  ( $m = +1$ ) transition has sufficient oscillator strength to appear in transmission. Note that in photoconductivity, all the impurity transitions are detected along with a series of oscillations at low magnetic fields. These are believed to correspond either to transitions to higher excited states or to Landau levels sweeping through the laser energy.

The structure shown in Fig. III-3 occurs at  $79\mu$  and reveals similar oscillations and impurity absorptions. Using field modulation to obtain the derivative, the triplet structure of the lines is clearly resolved, the magnetic field being measured to one part in  $10^3$  by NMR in Al<sup>27</sup>. The detail is shown in expanded form in Fig. III-4 and the results are summarized in Table III-1. The independence of the peak separations from field and wavelengths indicates that the energy shifts occur in the relatively field-insensitive 1s-states. Since the central cell corrections are largest for the spherical 1s-states, this tends to support our hypothesis.

An extremely narrow cyclotron resonance absorption line ( $\omega\tau \approx 40$ ) was also observed at 337 and  $311\mu$  in the course of these studies. After incorporating corrections for nonparabolicity, a value of  $m^* = 0.06649 \pm 0.00003$  is determined. This confirms earlier measurements<sup>20</sup> and is believed to be an order of magnitude more precise than previously obtained.<sup>21</sup>

---

<sup>†</sup> Francis Bitter National Magnet Laboratory, M.I.T.



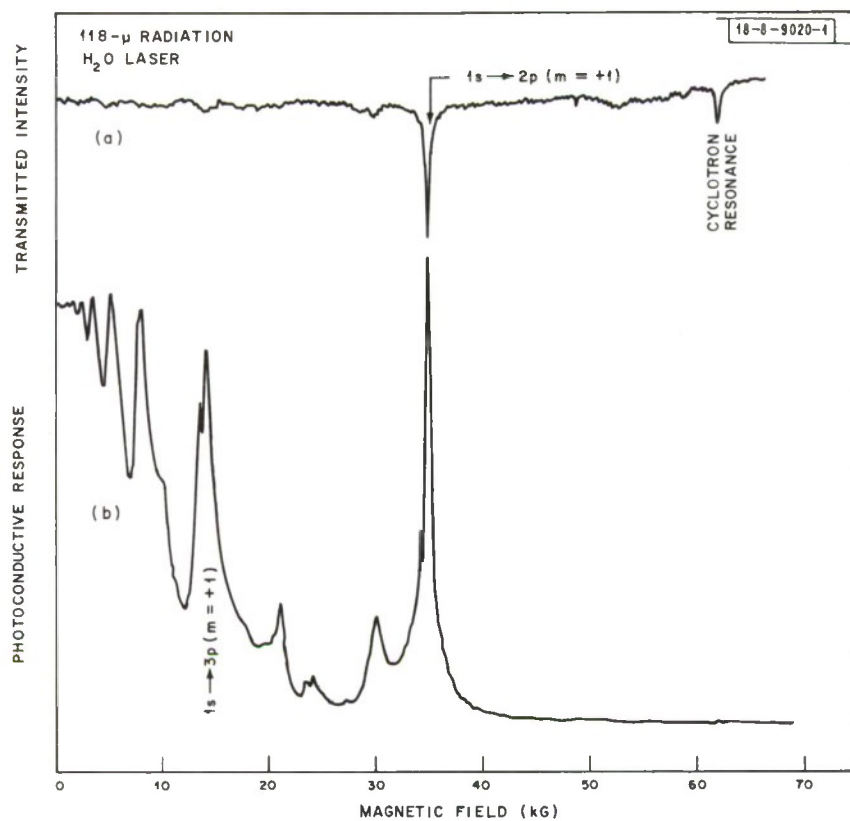


Fig. III-2. Recorder traces in GaAs at 4.2°K and 118  $\mu$  as a function of magnetic field: (a) absorption spectrum; (b) simultaneous photoconductivity (bias = 0.5  $\mu$ A).

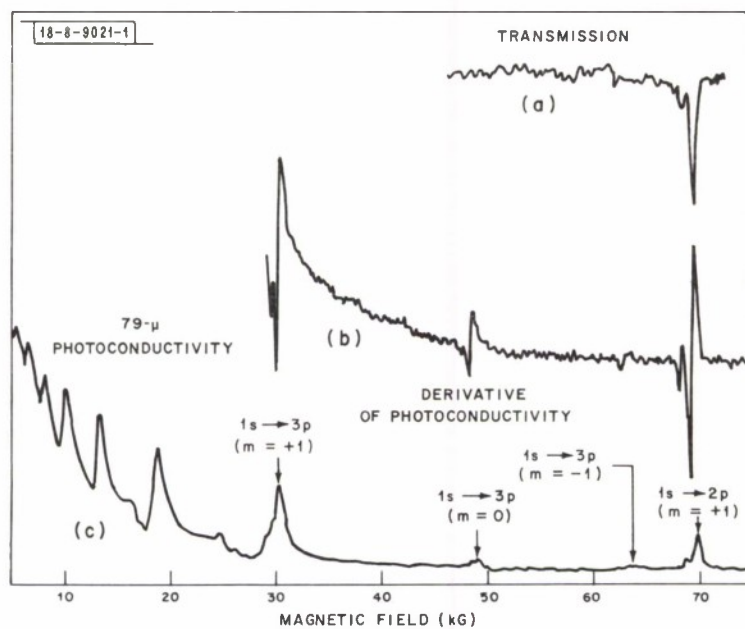


Fig. III-3. Recorder traces in GaAs at 4.2°K and 79  $\mu$ s as a function of magnetic field: (a) transmission showing the  $1s \rightarrow 2p$  ( $m = +1$ ) hydrogenic impurity transition; (b) derivative of photoconductivity obtained in field modulation; (c) photoconductivity (bias = 0.5  $\mu$ A).

# Section III

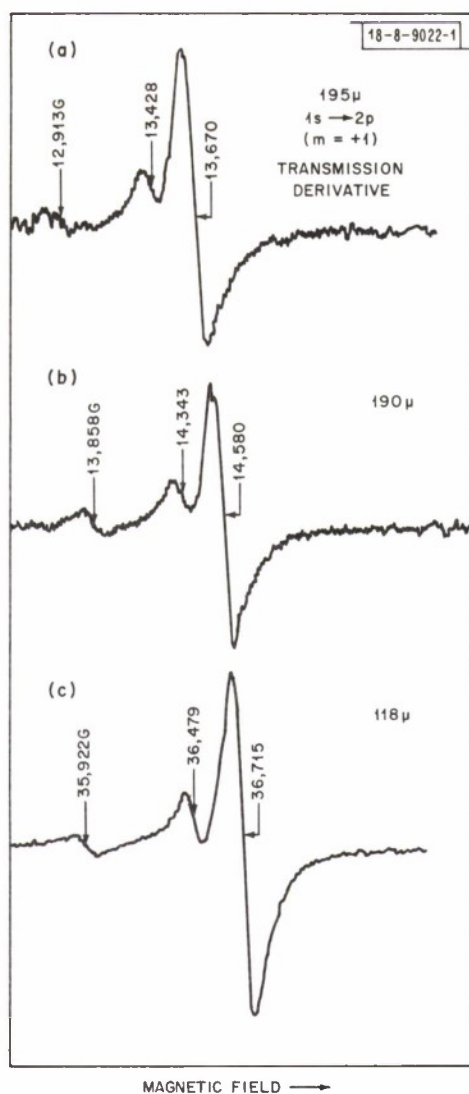


Fig. III-4. Recorder traces in GaAs at 4.2°K as a function of magnetic field of transmission derivatives of the  $1s \rightarrow 2p$  ( $m = +1$ ) transition at (a) DCN; (b) DCN; (c)  $H_2O$ . (Consistent results are obtained at 79  $\mu$ .)

TABLE III-1		
SPLITTING OF $1s \rightarrow 2p$ ( $m = +1$ ) TRANSITION; A, B AND C REFER TO THE PEAKS OF FIG. III-4		
Wavelength ( $\mu$ )	$\Delta$ (A-B) (gauss)	$\Delta$ (A-C) (gauss)
195	$242 \pm 20$	$757 \pm 20$
190	237	722
118	236	793

The accuracy achievable by using infrared lasers in combination with magnetic field modulation promises to provide a definitive test of the hydrogenic model applied to impurity transitions. Preliminary results indicate agreement between theory<sup>22</sup> and experiment for the  $1s \rightarrow 2p$  ( $m = +1$ ) transition to be better than 0.1 percent. This work is currently being extended to the  $2p$  ( $m = 0$ ) and  $3p$ -states.

H. Fetterman    P. E. Tannenwald  
J. Waldman    G. E. Stillman  
D. M. Larsen

## 6. Lattice Effects in the Localized State

The role of the lattice in a narrow-band insulator is investigated with the following Hamiltonian:

$$H = I \sum_i n_{i\uparrow} n_{i\downarrow} + \sum_q \omega_q a_q^\dagger a_q + \sum_{q,i} V_q \left( a_q e^{i\vec{q} \cdot \vec{R}_i} - a_q^\dagger e^{-i\vec{q} \cdot \vec{R}_i} \right) (n_{i\uparrow} + n_{i\downarrow}) \quad (\text{III-5})$$

The first term describes the usual intrasite Coulomb repulsion, the second term describes the free phonon field, and the third term describes the coupling<sup>†</sup> between the phonons and electrons. The parameters  $\omega_q$  and  $V_q$  can be fairly general functions of the wave vector  $q$ . If the first term of Eq. (III-5) is replaced by an electron kinetic energy term, then the equation has a Fröhlich-like form in which a single free electron interacts with a phonon field. Equation (III-5) is designed to study the opposite limit in which the electron kinetic energy is ignored compared with a strong Coulomb repulsion.

The statistical mechanics of  $I \sum_i n_{i\uparrow} n_{i\downarrow}$  is easily carried out and the free energy is an analytic function of its parameters. The properties of Eq. (III-5) are not as simply calculated, but the canonical transformation

$$b_q^\dagger = a_q^\dagger + \frac{V_q}{\omega_q} \sum_i e^{-i\vec{q} \cdot \vec{R}_i} (n_{i\uparrow} + n_{i\downarrow})$$

allows one to transform Eq. (III-5) into

$$H = I \sum_i n_{i\uparrow} n_{i\downarrow} + \sum_q \omega_q b_q^\dagger b_q + \sum_{i,j} v_{ij} (n_{i\uparrow} + n_{i\downarrow}) (n_{j\uparrow} + n_{j\downarrow}) \quad (\text{III-6})$$

where

$$-v_{ij} \equiv \sum_q \frac{|V_q|^2}{\omega_q} \exp[i\vec{q} \cdot (\vec{R}_i - \vec{R}_j)]$$

<sup>†</sup> This form assumes first-order deviation of the ions from the equilibrium positions. For a derivation, see Ref. 23.



### Section III

Equation (III-6) has the interesting feature that the electron-phonon coupling Hamiltonian has been replaced by an electron-electron interaction term with coupling parameter  $v_{ij}$ . In this representation, the eigenstates are seen to be products of free phonon wave functions with single Slater determinants of Wannier functions. The partition function is also a product of a phonon contribution and an electron contribution, but, although the eigenstates are known, the evaluation of the partition function for the electronic part is nontrivial for general  $v_{ij}$ .

We consider the special case  $v_{ij} = v_0 \delta_{ij} + v_1 f_{ij}$ , where  $v_1 > 0$  and  $f_{ij} = 1/2$  for  $i, j$  nearest-neighbors and  $f_{ij} = 0$  otherwise. The electronic part of the Hamiltonian is then

$$H_e = (I + 2v_0) \sum_i n_{i\uparrow} n_{i\downarrow} + v_1 \sum_{i,j} f_{ij} (n_{i\uparrow} + n_{i\downarrow}) (n_{j\uparrow} + n_{j\downarrow}) + v_0 \sum_i (n_{i\uparrow} + n_{i\downarrow}) \quad (III-7)$$

The third term of Eq. (III-7) represents a constant shift of the energy levels and will not be discussed here. When the number of electrons is equal to the number of sites, the first and second terms separately describe quite different ground states. The ground state of the first term alone has one electron per site and describes a Mott insulator. However, for the second term alone, the ground state would have half the sites doubly occupied with no two adjacent sites unoccupied<sup>24</sup> (we assume a lattice in which the  $z$  nearest-neighbors of any given site lie on a different sublattice). Furthermore, the ground-state entropy for the first term is  $Nk \ln 2$ , whereas for the second term it is zero. It seems possible that Eq. (III-7) will exhibit a phase transition as a function of temperature for  $v_1$  sufficiently large that the ground state will be dominated by the second term of Eq. (III-7).

This critical value of  $v_1$  is estimated in the thermal Hartree-Fock approximation, in which one looks for a solution with  $\langle n_i \rangle \neq \langle n_j \rangle$  for  $i$  and  $j$  on different sublattices. One obtains that  $v_1 > (I + 2v_0)/2z$  is a necessary and sufficient condition that such a solution exists. Above a critical temperature, given by  $kT_c = (1/4) [2zv_1 - (I + 2v_0)]$ , one has  $\langle n_i \rangle = \langle n_j \rangle$  for all  $i$  and  $j$  and the phase transition is second order.

Exact analysis of Eq. (III-7) for the linear chain yields that there is no phase transition in one dimension, as expected.

The effects of the lattice when strong Coulomb correlations are present is under further investigation.

R. A. Bari

#### 7. Existence of Exact Quasi-Particles for Systems of Interacting Particles

We prove and discuss the following theorem. Let a complete orthonormal set  $\{\dots \Phi_n \dots\}$  of many-particle states be defined as all possible products of fermion creation operators  $a_1^\dagger, \dots, a_K^\dagger$ , and their boson counterparts  $b_1^\dagger, \dots, b_L^\dagger$ , acting on the vacuum  $|0\rangle_{ab}$ ,

$$\Phi_n = \prod_i^{(n)} a_i^\dagger \prod_j^{(n)} b_j^\dagger |0\rangle_{ab} \quad (III-8)$$

where

$$\prod_i^{(n)} a_i^\dagger = a_{i_1}^\dagger, a_{i_2}^\dagger, \dots \quad (i_1 < i_2 < \dots) \quad ;$$

$$\prod_j^{(n)} b_j^\dagger = b_{j_1}^\dagger, b_{j_2}^\dagger, \dots \quad (i_1 < i_2 < \dots) \quad ;$$

and

$$a_i |0\rangle_{ab} \equiv b_j |0\rangle_{ab} \equiv 0 \quad . \quad (\text{III-9})$$

( $n$  denotes the particular set of  $a_i$  and  $b_j$  involved in the product.) Let  $H$  be a Hamiltonian which can be written in terms of the  $\dots a_i, a_i^\dagger, \dots, b_j, b_j^\dagger, \dots$ , and assume that the eigenstates of  $H$  are denumerable. Then there exists a new set of fermion (A) and boson (B) operators,

$$\begin{aligned} A_i &= U a_i U^{-1} \\ B_j &= U b_j U^{-1} \end{aligned} \quad (\text{III-10})$$

where  $U$  is a unitary operator, such that when the  $\dots a_i, \dots, b_j, \dots$  are eliminated from  $H$  in favor of the  $\dots A_i, \dots, B_j, \dots$ ,  $H$  involves the latter only through the number operators  $N_{iA} = A_i^\dagger A_i$ ,  $N_{iB} = B_i^\dagger B_i$ :

$$H = H(\dots, N_{iA}, \dots, N_{jB}, \dots) \quad . \quad (\text{III-11})$$

Also, all the eigenstates  $\Psi_n$  of  $H$  can each be written as

$$\Psi_n = \prod_i^{(n)} A_i^\dagger \prod_j^{(n)} B_j^\dagger |0\rangle_{AB} \quad . \quad (\text{III-12})$$

$|0\rangle_{AB}$  is the "AB vacuum" defined analogously to Eq. (III-10).

Since  $\{\dots \Phi_n \dots\}$  and  $\{\dots \Psi_n \dots\}$  both are complete sets of orthonormal states, they must be related by a unitary operator<sup>‡</sup>  $\bar{U}$

$$\Psi_n = \bar{U} \Phi_n \quad . \quad (\text{III-13})$$

Combining Eqs. (III-8) and (III-13), we see that

$$\Psi_n = \bar{U} a_i^\dagger \bar{U}^{-1} \bar{U} a_{i_2}^\dagger \bar{U}^{-1} \dots \bar{U} b_{j_1}^\dagger \bar{U}^{-1} \dots \bar{U} b_{j_{\max}}^\dagger \bar{U}^{-1} \bar{U} |0\rangle_{ab} \quad . \quad (\text{III-14})$$

<sup>‡</sup> This follows from the assumed denumerability of the energy eigenfunctions. For a system of fermions only, this denumerability automatically occurs for  $L$  finite.

### Section III

Identifying  $\bar{U} = U$  and  $U |0\rangle_{ab} = |0\rangle_{AB}$ , we see that Eq. (III-14) gives Eq. (III-12). But, with  $C = A$  or  $B$ ,  $c = a$  or  $b$ ,

$$N_{iC} |0\rangle_{AB} = U c_i^\dagger c_i U^{-1} U |0\rangle_{ab} = U c_i^\dagger c_i |0\rangle_{ab} = 0$$

which shows that  $|0\rangle_{AB}$  is the AB vacuum. To establish Eq. (III-11), we note that the operators in Eq. (III-12) are eigenfunctions of the number operators  $\dots N_{iA} \dots N_{jB} \dots$ , which form a complete set of commuting operators. Since Eq. (III-12) operators are also eigenfunctions of  $H$ , it follows that  $H$  is completely determined by a function of the  $\dots N_{iA} \dots N_{jB} \dots$ , i.e., Eq. (III-11) follows.

We shall refer to the  $A_i, B_j$  as exact quasi-particle operators.

Because the  $\Phi_n$  are to a considerable extent arbitrary, it might appear that the  $A_i$  and  $B_j$  are also arbitrary. In fact, however, to the extent that the exact energy eigenstates  $\Psi_n$  are unique and aside from relabeling, the  $A_i$  and  $B_j$  are unique: Suppose instead of the  $\Phi_n$ , we consider a new basis

$$\Phi'_n = \prod a_i'^\dagger b_j'^\dagger |0\rangle_{a'b'} \quad (III-15)$$

where

$$a_i = V a_i' V^{-1}, \quad b_j = V b_j' V^{-1} \quad (III-16)$$

and  $V$  is unitary. ( $|0\rangle_{a'b'} = V^{-1} |0\rangle_{ab}$ .) Following the previous procedure by writing  $\Psi_n = U' \Phi'_n$ , we would have obtained the analogy of Eq. (III-12) with  $A_i' = U' a_i' U'^{-1}$  and  $B_j' = U' b_j' U'^{-1}$  replacing  $A_i$  and  $B_j$ . But, from Eqs. (III-8) and (III-16) we see that  $\Phi_n = V \Phi'_n$  so that  $\Psi_n = UV \Phi'_n$  and, therefore,  $U' = UV$ . Hence,  $A_i' = UV a_i' V^{-1} U^{-1} = U a_i U^{-1} = A_i$  and, similarly,  $B_i' = B_i$ .

The lifetimes of these exact quasi-particles are clearly infinite, since adding a quasi-particle to an energy eigenstate  $\Psi_n$  (e.g., constructing the state  $A_i^\dagger \Psi_n$ ) gives an energy eigenstate, according to Eq. (III-12), which of course does not decay. On the other hand, the Hamiltonian Eq. (III-11) is not generally a linear function of the  $N_{iA}$  and  $N_{jB}$ , so that there are interactions between these exact quasi-particles. Thus, interactions between quasi-particles need not lead to finite lifetimes, in contradiction to what some have thought.<sup>25</sup>

That the lifetimes of all the exact quasi-particles are infinite seems to contradict a point which is emphasized in many textbooks.<sup>25,26</sup> One might guess that this occurred because we have defined quasi-particles differently. In fact, this is not the case, according to Chapter I of Ref. 26 where the definition coincides with ours.<sup>†</sup> Another possibility is that, for macroscopic systems, there might be convergence problems that occur in the process of taking the thermodynamic limit and/or the limit of an infinite number of basis states (so that, for example, our assumed

<sup>†</sup> However, later in Ref. 26 (Chapter 3, Sec. d), a quasi-particle lifetime is defined as the lifetime of a state  $a_i^\dagger \Psi_0$  where  $\Psi_0$  is the ground state of the interacting system. This state ( $a_i^\dagger \Psi_0$ ), it seems to us, should be called a bare particle introduced into the interacting system in its ground state; it is certainly different from the definition of a quasi-particle given in Chapter 1 of Ref. 26.

denumerability of the  $\Psi_n$  might be violated in a serious way)<sup>27</sup>; clearly, this is the only possibility for violating our conclusion about the existence of exact quasi-particles. It is an important possibility and is being studied.

T. A. Kaplan

## B. MAGNETISM

### 1. Magnetic Properties of EuO

As reported in the previous quarterly report,<sup>28</sup> we determined the critical magnetic exponents of EuO, obtaining  $\beta = 0.368 \pm 0.005$ ,  $\delta = 4.46 \pm 0.10$ , and  $\gamma = 1.29 \pm 0.01$ . These values agree, within experimental error, with the relationships predicted by scaling theory. In further agreement with scaling theory, it has been established that for  $h = H\epsilon^{-\beta\delta}$  and  $m = \sigma\epsilon^{-\beta}$ , where  $H$  is the magnetic field in the sample,  $\sigma$  is the magnetic moment, and  $\epsilon = |T - T_c|/T_c$ ,  $h$  can be expressed as a function of  $m$  alone. However, the form of  $h(m)$  is different for  $T$  above and below  $T_c$ . In attempting to see if a single equation of state could be established for EuO which is applicable both above and below  $T_c$ , we found that the linear model of Schofield, *et al.*<sup>29</sup> represented at least a good approximation throughout the critical temperature region.

In addition, our experimental results were analyzed in terms of the high-temperature series expansion for fcc lattices with nearest- ( $J_1$ ) and next-nearest-neighbor ( $J_2$ ) interactions to determine the values of these interactions. From our analysis, we conclude that the next-nearest-neighbor interaction is ferromagnetic, with  $J_2/J_1 = 0.5 \pm 0.2$  and  $J_1/k = 0.53 \pm 0.05^\circ\text{K}$ . Previously reported results, which were based on low-temperature ( $T < 4.2^\circ\text{K}$ ) NMR<sup>30</sup> and specific-heat measurements<sup>31</sup> have indicated that  $J_2$  is antiferromagnetic with  $J_2/J_1 \approx -0.12$ . This value is incompatible with our measurements.

N. Menyuk  
K. Dwight  
T. B. Reed

### 2. Electron Spin Waves in Nonmagnetic Conductors: Self-Consistent Field Theory

A general treatment of the electrodynamic response of a quantum many-electron gas in a nonmagnetic conducting solid immersed in an applied magnetic field has been derived.<sup>32</sup> Self-consistent field theory of the equation of motion of the one-electron density matrix was used in such a way as to include, from the outset, one-electron effects such as complex energy band structure, spin-orbit coupling, and spin paramagnetism. This treatment specifically omits exchange effects such as those encountered in an extended random phase approximation or Landau Fermi liquid theory. The aim was to study the properties of wave propagation in the gas, looking for spin waves and/or characteristic effects which uniquely involve the spin degree of freedom and the paramagnetism of the equilibrium state. The derived results contain terms which have been neglected previously and terms which do not evolve from a simple generalization of previous treatments of the quantum dielectric theory of a Fermi gas. There are interesting spin effects in the plasma wave properties both with and without spin-orbit mixing of the one-electron states. In an effective mass approximation for the one-electron states, it was shown that there are resonances and cutoffs associated with electron spin resonance in the transverse wave propagation (both perpendicular and parallel to the magnetic field). For spin-orbit mixed states, one finds zeros of the longitudinal dielectric constant (for long wavelength) near the electron spin-flip frequency.<sup>33</sup> The mechanism for the spin wave associated with this zero is a correlation of the



### Section III

motion of electrons with "opposite spins" by the long-range Coulomb field through the spin-orbit coupling of the crystalline eigenstates. A manuscript giving the results of this calculation has been submitted for publication.

F. A. Blum

## C. LASER SCATTERING AND NONLINEAR EFFECTS

### 1. Light Scattering from Plasmons in InSb

Although inter-Landau-level light scattering from conduction electrons in indium antimonide in a strong magnetic field has been observed,<sup>34</sup> no plasmon scattering has been reported (either with or without a magnetic field). Furthermore, light scattering from plasmons in the related material indium arsenide has been observed<sup>35</sup> using a 10- $\mu$  laser, even though the scattering cross section is expected to be smaller than that for InSb. The latter experiments<sup>35</sup> also had the peculiar property of not yielding any evidence of plasmon-phonon coupling. Only one scattering peak was observed, and only at electron densities such that the uncoupled plasma frequency was well below the longitudinal optical phonon frequency. Using a high-power 5- $\mu$  carbon monoxide laser, we have observed<sup>36</sup> inelastic light scattering from plasmons (no magnetic field) in n-type InSb, and find measurable scattering for carrier concentrations  $n_e$  both above and below the region of strong coupling between the plasmon and the longitudinal optical phonon. No pure phonon scattering peaks are observed in samples with very low  $n_e$ . A single plasmon peak is observed for moderate  $n_e$ . Two peaks are observed for  $n_e$  in the region of strong coupling. The density and polarization dependence of the scattering indicate that the coupling to charge density fluctuations is the dominant scattering mechanism.

The long wavelength eigenfrequencies of the coupled plasmon-phonon modes are given by the zeros of the longitudinal dielectric function.<sup>37</sup> Figure III-5 shows a plot (solid lines) of the two roots  $\omega_+$  and  $\omega_-$  as a function of  $n_e$  for conduction electrons in InSb. We have used<sup>†</sup>  $\epsilon_\infty = 16.0$ ,  $\omega_{LO} = 193.8 \text{ cm}^{-1}$ , and  $\omega_{TO} = 181.4 \text{ cm}^{-1}$ . Also, because of the strong nonparabolicity of the InSb conduction band, we have used for the plasma frequency,

$$\omega_p^2 = \frac{4\pi n_e e^2}{m_d \epsilon_\infty}$$

where

$$m_d = \left[ \frac{p}{\partial \epsilon / \partial p} \right]_{p=p_F}$$

is the density-of-states effective mass evaluated at the Fermi surface. This mass varies significantly<sup>38</sup> from about 0.015  $m$  for  $n_e = 10^{16} \text{ cm}^{-3}$  to 0.022  $m$  for  $n_e = 2 \times 10^{17} \text{ cm}^{-3}$ . Also shown in Fig. III-5 are data points for the location of the experimental inelastic scattering peaks.

No scattering was detectable at  $\omega_+$  for the samples with lowest  $n_e$ . As  $n_e$  was increased, the  $\omega_+$  branch first occurred with a strength  $\sigma_+$  very weak relative to that of the lower branch ( $\sigma_-$ ), and then increased substantially so that  $(\sigma_+/\sigma_-) \approx 1$ . Experiments in a sample with  $n_e$  higher

<sup>†</sup> The phonon frequencies used in this report are those determined by Raman scattering,  $\omega_{LO} = 193.8 \pm 0.5 \text{ cm}^{-1}$  and  $\omega_{TO} = 181.4 \pm 0.5 \text{ cm}^{-1}$ ; K. W. Nill and A. Mooradian, Bull. Am. Phys. Soc. **13**, 1658 (1968) and (to be published). These values are close to, but not identical with other values in the literature. See M. Hass in *Semiconductors and Semimetals*, Vol. 3, R. K. Willardson and A. C. Beer, eds. (Academic Press, New York, 1967), p. 3, and references therein. The results here are not sensitive to the specific value used.

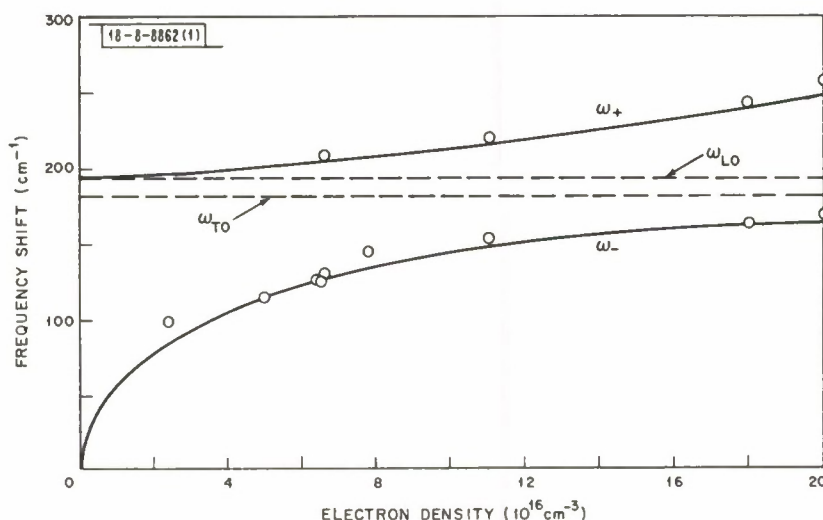


Fig. III-5. Frequency shift of coupled plasmon-phonon modes vs electron density. Solid curves are theoretical, and circles are experimental data points.

than that shown in Fig. III-5 yielded only very weak scattering from the  $\omega_+$  mode, and no scattering from the  $\omega_-$  mode.

F.A. Blum  
A. Mooradian

## 2. Raman Scattering and Lattice Dynamics of Tellurium

The lattice vibrations of trigonal tellurium have been studied recently by neutron scattering<sup>39</sup> and infrared reflectivity.<sup>40</sup> Complementary data obtained by Raman scattering are presented here. Tellurium crystallizes with space group  $D_3^4$  (or  $D_3^6$ ) having three atoms per unit cell arranged helically about the c-axis. The symmetries of the optical phonons at the center of the Brillouin zone are one Raman active  $\Gamma_1$ -singlet, one infrared active (extraordinary ray)  $\Gamma_2$ -singlet, and two Raman and infrared active (ordinary ray)  $\Gamma_3$ -doublets. Although tellurium is homonuclear, there is a dynamic charge associated with the  $\Gamma_2$ - and  $\Gamma_3$ -modes<sup>41</sup>; the strength of the ionic character has been measured in the reststrahlen.<sup>40</sup> This effective charge is also measured in the Raman experiment by the splitting of the  $\Gamma_3$ -doublet, for wavevector  $\vec{q} \perp c$ -axis, into modes of longitudinal and transverse polarization. Also, for  $\vec{q} \parallel c$ -axis, the purely transverse  $\Gamma_3$ -doublet is split proportional to  $q$  as a consequence of the screw symmetry of the lattice.<sup>42</sup> This dispersion is measurable by high-resolution Raman scattering since phonon wavevectors up to  $4\pi|n + ik|/\lambda$  may be probed, where  $n$  and  $k$  are the real and imaginary parts of the refractive index, and  $\lambda$  is the incident light wavelength. Furthermore, the Raman scattering selection rules unambiguously determine the phonon symmetries and orderings near the zone center, and indicate the relative contributions of the deformation potential and the electro-optic effect to the electron-phonon interaction. A summary of the Raman shifts and linewidths (full width at half maximum) in tellurium at two temperatures is presented in Table III-2. The incident argon laser wavelength is 5145 Å; the inelastically surface backscattered light is analyzed in a Spex 1400 tandem spectrometer and is detected by an uncooled FW130 photomultiplier. Repetitively scanned data are accumulated in a multichannel analyzer to enhance the signal-to-noise ratio. Typical polarized spectra taken from a surface normal to the c-axis are given in

## Section III

TABLE III-2				
RAMAN SCATTERING DATA IN TELLURIUM				
Mode	Temperature 295°K		Temperature 90°K	
	Frequency (cm <sup>-1</sup> )	Linewidth (cm <sup>-1</sup> )	Frequency (cm <sup>-1</sup> )	Linewidth (cm <sup>-1</sup> )
$\Gamma_{3TO}$	$92.2 \pm 0.5$	$4.8 \pm 0.5$	$95.2 \pm 0.5$	$1.5 \pm 0.5$
$\Gamma_{3LO} - \Gamma_{3TO}$	$12 \pm 2$	—	—	—
$\Gamma_{3TO}^+ - \Gamma_{3TO}^-$	—	—	$-0.60 \pm 0.1$	—
$\Gamma_1$	$120.4 \pm 0.5$	$6.4 \pm 0.5$	$123.4 \pm 0.5$	$1.5 \pm 0.5$
$\Gamma_{3TO}$	$140.7 \pm 0.5$	$2.8 \pm 0.5$	$142.9 \pm 0.5$	$0.4 \pm 0.4$
$\Gamma_{3LO} - \Gamma_{3TO}$	—	—	$0.6 \pm 0.2$	—
$\Gamma_{3TO}^+ - \Gamma_{3TO}^-$	—	—	$-0.26 \pm 0.1$	—

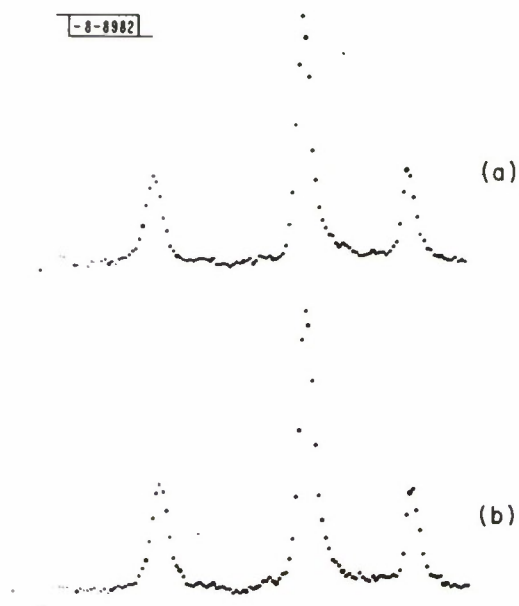


Fig. III-6. Raman backscattering spectrum of tellurium at 90°K: (a)  $z(+, x + y) \bar{z}$ ; (b)  $z(-, x + y) \bar{z}$ .

Fig. III-6(a-b). The small shifts of the two  $\Gamma_3$ -modes, denoted  $\Gamma_{3\text{TO}}^+ - \Gamma_{3\text{TO}}^-$ , are in the same direction contrary to the interpretation of the neutron data.<sup>39</sup> A lattice dynamics calculation based on a symmetrized Fourier expansion technique is being carried out to correlate the existing data on tellurium.

A. S. Pine  
G. F. Dresselhaus

### 3. Resonant Coupling of Landau Levels via LO Phonons in Polar Semiconductors and Its Effect on Landau Level Raman Scattering from Semiconductor Plasmas

The Green's-function method for studying the resonant coupling of Landau levels via LO phonons is re-examined and the approximations made therein are justified. Coupling between the  $n = 2$  and  $n = 1$  Landau levels plus one LO phonon continuum is investigated under the condition that the cyclotron frequency  $\omega_c$  is nearly equal to the LO phonon frequency  $\omega_o$ . Since the  $n = 1$  Landau level has been resonantly coupled to the  $n = 0$  Landau level plus one LO phonon continuum under the same condition, novel features of the electron energy spectrum appear. It is shown that the pinning effect that occurs for the  $n = 1$  Landau level exists also for the  $n = 2$  level. The cross section for the inelastic light scattering from electron plasmas in polar semiconductors under the influence of a DC magnetic field is calculated approximately with the inclusion of electron-phonon polar interaction. The effect of both Coulomb and electron-phonon interactions on the momentum matrix elements occurring in the calculation is neglected, but is kept in the evaluation of the correlation function of a generalized pair operator. The results of scattering from single-particle excitations between the  $n = 0$  and  $n = 2$  Landau levels exhibit the effect of the resonant coupling between the  $n = 2$  and  $n = 1$  levels via LO phonons. However, for scattering from collective modes such as the coupled LO phonon-magnetoplasma mode and the Bernstein modes, the possibility of observing similar resonant coupling effects is ruled out.

K. L. Ngai

### 4. Two-Wave Nonlinear Mixing in GaAs

In relation to the two-wave frequency-mixing experiment in GaAs (Ref. 43), theoretical calculations have been made to understand the effects various mechanisms have on the response time associated with the IF (difference) frequency. The experiment was carried out first with two waves at 4 mm (75 GHz) and then at 0.337 mm (890 GHz) which corresponds to 3.68 meV, a little less than the ( $1s \rightarrow 2p$ ) transition (4.4 meV) for the shallow donor state.<sup>44</sup> Detection of the IF frequency at about 1 MHz was made by photoconduction instead of by emitted radiation as in related experiments<sup>45</sup> at  $10\mu$  with a  $\text{CO}_2$  laser.

Calculation based on nonlinearity due to the energy dependences of carrier lifetime, momentum, and energy relaxation times, and due to the photoionization process (if any), gives the following expression for the IF current density,  $J(\omega_3)$ , with  $\omega_3 = \omega_1 - \omega_2$  (the difference of the two frequencies in the source)

$$J(\omega_3) = NV_o \frac{4e^2 \tau_P E(\omega_1) E(\omega_2)^* \tau_E G}{3kT_e m [1 - s\delta + i\omega_3 \tau_E]} \left[ \frac{n/2}{1 + i\omega_3 \tau_P} + \frac{q}{1 + i\omega_3 \tau_N} \right] + V_o \frac{cE(\omega_1) E(\omega_2)^* \tau_N \alpha}{2\pi(1 + i\omega_3 \tau_N) \hbar \omega} \quad (\text{III-17})$$



### Section III

where  $N$  is the carrier density,  $V_0 = -eE_0\tau_P/m$ , the drift velocity,  $c$  is the speed of light,  $\alpha$  is the effective photoionization absorption coefficient at  $\omega = \omega_1 \approx \omega_2$ , and  $G \cong (1 + \omega^2\tau_P^2)^{-1}$ . The momentum, conduction band energy relaxation time and carrier recombination time are  $\tau_P$  ( $\sim 10^{-12}$  sec) for cold electrons,  $\tau_E'$  ( $\sim 10^{-7}$  sec) for hot electrons just before breakdown threshold, and  $\tau_N$  ( $\sim 10^{-8}$  sec) for cold electrons, respectively.  $\tau_E^{-1} = \tau_E'^{-1} + \tau_N^{-1}$ . Their dependences on electron temperature are given by

$$\tau_P \propto T_e^{n/2}, \quad \tau_E' \propto T_e^{s'}, \quad \tau_N \propto T_e^q \quad \text{and} \quad \tau_E \propto T_e^s$$

where  $n = 3$  for the dominant ionized impurity scattering at 4°K (Ref. 46),  $s' = 1/2$  for piezoelectric potential scattering and  $-1/2$  for deformation potential scattering,<sup>47</sup>  $q = 1.8$  experimentally<sup>48</sup> and  $\sim 1.5$  theoretically.<sup>49</sup> In order to calculate  $J(\omega_3)$ , one has to know the electron temperature and the time constants dependent on it. These can be determined from  $P$ , the power per unit volume delivered to the sample,

$$P = p_{\pm} N \delta \left( \frac{T_e}{T_0} \right)^{1 \pm 1/2} \quad (\text{III-18})$$

where  $T_0$  is the lattice temperature, the coefficient  $p_{\pm}$  may be found in Ref. 47, and the upper sign is for deformation potential scattering while the lower sign is for piezoelectric potential scattering.  $\delta = 1 - T_0/T_e$  in Eqs. (III-17) and (III-18).

Carrier density modulation manifests itself in the second term in the bracket of Eq. (III-17) due to the energy dependence of carrier lifetime, and in the last term due to nonlinearity of direct photoionization or photoexcitation followed by thermal ionization. These effects, together with the nonlinearity associated with the energy-dependent energy relaxation time, were not considered previously<sup>50,51</sup> as frequency-mixing mechanisms because the frequencies involved earlier were much higher than  $\tau_E^{-1}$  or  $\tau_N^{-1}$ , leaving only  $\tau_P^{-1}$  of importance, as in the first term of Eq. (III-17). Conduction band nonparabolicity effects<sup>50</sup> were also computed, but were found to be smaller by a factor of  $kT_e\tau_P/E_g\tau_E \sim 10^{-6}$  for this low-frequency case.

To compare with the experimental results, we note that at the longer wavelength,  $\lambda = 4$  mm ( $\hbar\omega \sim 0.3$  meV), no photoionization can take place and  $\alpha = 0$ . The electrons are sufficiently hot for the IF response time to be characterized by  $\tau_E \sim 10^{-7}$  sec, since  $\tau_N > \tau_E' \gg \tau_P$  in Eq. (III-17) if piezoelectric potential scattering dominates in GaAs as in InSb (Ref. 52). In addition,  $\tau_E$  is seen to be proportional to  $T_e^s$  and thus should increase with bias current by Eq. (III-18). This is in qualitative agreement with the experiment. At the shorter wavelength ( $\lambda = 0.337$  mm),  $\hbar\omega \sim 3.68$  meV and photoexcitation followed by fast thermal ionization can occur. With about  $10^{13}$  neutral donors/cm<sup>3</sup> (Ref. 44),  $\alpha \cong 0.1$  cm<sup>-1</sup> at this wavelength, and with  $N \cong 10^8$ /cm<sup>3</sup> (Ref. 44), one can show that the last term in Eq. (III-17) is comparable to the first two terms, while  $\tau_E \cong \tau_N$  for cold electrons, thus yielding an IF response time that is characterized by  $\tau_N \sim 10^{-8}$  sec. This possibly explains why a much shorter response time ( $\tau < 4 \times 10^{-8}$  sec) was observed at 0.337 mm than at 4 mm.

An extension of the two-wave mixing experiments to three-wave mixing is planned in which the difference of two laser frequencies ( $\lambda \sim 300 \mu$ ) is to be mixed with a microwave signal at  $\sim 75$  GHz, giving an IF signal at about 1 MHz. Since the response is to be detected via photoconduction, the problem of transferring the IF modulation to the conduction electrons is being considered.

B. Y. Lao  
M. M. Litvak

## REFERENCES

1. E. J. Johnson and D. H. Dickey, Phys. Rev. B 1, 2676 (1970).
2. L. M. Roth, B. Lax and S. Zwerdling, Phys. Rev. 114, 90 (1959).
3. R. A. Isaacson, Phys. Rev. 169, 312 (1968).
4. J. Callaway, J. Electron. 2, 330 (1957).
5. M. Cardona, J. Phys. Chem. Solids 24, 1543 (1963).
6. F. Herman, R. L. Kortum, C. D. Kuglin, J. P. Van Dyke and S. Skillman, Methods in Computational Physics, edited by B. Alder, S. Fernback and M. Rotenberg (Academic Press, New York, 1968).
7. F. H. Pollak, M. Cardona, C. W. Higginbotham, F. Herman and J. P. Van Dyke, Phys. Rev. (to be published).
8. B. L. Booth and A. W. Ewald, Phys. Rev. 168, 796 (1968).
9. S. H. Groves, C. R. Pidgeon, A. W. Ewald and R. J. Wagner, J. Phys. Chem. Solids 31, 2031 (1970).
10. D. H. Dickey, E. J. Johnson and D. M. Larsen, Phys. Rev. Letters 18, 599 (1967), DDC AD-658789.
11. E. J. Johnson and D. H. Dickey, Phys. Rev. B 1, 2676 (1970).
12. M. Haas and B. W. Henvis, J. Phys. Chem. Solids 23, 1099 (1962).
13. D. H. Dickey and D. M. Larsen, Phys. Rev. Letters 20, 65 (1968), DDC AD-669206.
14. B. D. McCombe and R. Kaplan, Phys. Rev. Letters 21, 756 (1968).
15. R. C. Brandt, D. M. Larsen, P. P. Crooker and G. B. Wright, Phys. Rev. Letters 23, 240 (1969), DDC AD-694139.
16. R. W. Davies and H. J. Zeiger, Proceedings of the 10th International Conference on the Physics of Semiconductors, Cambridge, Massachusetts, 17-21 August 1970 (to be published).
17. J. W. Hodby, Solid State Commun. 7, 811 (1969).
18. C. J. Summers, R. Dingle and D. E. Hill, Phys. Rev. B 1, 1603 (1970).
19. C. M. Wolfe, G. E. Stillman and E. B. Owens, J. Electrochem. Soc. 117, 129 (1970), DDC AD-703487.
20. G. E. Stillman, C. M. Wolfe and J. O. Dimmock, Solid State Commun. 7, 921 (1969), DDC AD-693903.
21. J. M. Chamberlain and R. A. Stradling, Solid State Commun. 7, 1275 (1969).
22. D. M. Larsen, J. Phys. Chem. Solids 29, 271 (1968), DDC AD-664919.
23. J. Bardeen and D. Pines, Phys. Rev. 99, 1140 (1955).
24. A similar situation has been encountered in T. A. Kaplan and P. N. Argyres, Phys. Rev. B 1, 2457 (1970).
25. For example, see A. A. Abrikosov, L. P. Gor'kov, and I. E. Dzyaloshinski, Methods of Quantum Field Theory in Statistical Physics (Prentice-Hall, New York, 1963), p. 17.
26. For example, see P. Nozieres, Interacting Fermi Systems (W. A. Benjamin, New York, 1964), p. 3.
27. See the discussions of N. M. Hugenholtz, Physica 23, 481 and 533 (1957).
28. Solid State Research Report, Lincoln Laboratory, M. I. T. (1970:2), pp. 55-57.
29. P. Schofield, J. D. Litster and J. T. Ho, Phys. Rev. Letters 23, 1098 (1969).
30. E. L. Boyd, Phys. Rev. 145, 174 (1966).
31. A. J. Henderson, Jr., G. R. Brown, T. B. Reed and H. Meyer, J. Appl. Phys. 41, 946 (1970).

### Section III

32. F. A. Blum, Bull. Am. Phys. Soc. 15, 273 (1970).
33. ———, Phys. Rev. Letters 23, 73 (1969), DDC AD-694146.
34. R. E. Slusher, C. K. N. Patel and P. A. Fleury, Phys. Rev. Letters 18, 77 (1967);  
C. K. N. Patel and E. D. Shaw, Phys. Rev. Letters 24, 451 (1970).
35. C. K. N. Patel and R. E. Slusher, Phys. Rev. 167, 413 (1968).
36. F. A. Blum and A. Mooradian, Proceedings of the 10th International Conference on the Physics of Semiconductors, Cambridge, Massachusetts, 17-21 August 1970 (to be published).
37. B. B. Varga, Phys. Rev. 137, A1896 (1965).
38. E. J. Johnson and D. H. Dickey, Phys. Rev. B 1, 2676 (1970).
39. B. M. Powell and P. Martel, Bull. Am. Phys. Soc. 15, 810 (1970), and private communication.
40. G. Lucovsky, R. C. Keezer and E. Burstein, Solid State Commun. 5, 439 (1967).
41. R. Zallen, Phys. Rev. 173, 824 (1968).
42. A. S. Pine and G. Dresselhaus, Phys. Rev. 188, 1489 (1969), DDC AD-707581.
43. H. Fetterman, P. E. Tannenwald and C. D. Parker, Proceedings of Symposium on Submillimeter Waves, New York, 1970.
44. G. E. Stillman, C. M. Wolfe and J. O. Dimmock, Solid State Commun. 7, 921 (1969), DDC AD-693903.
45. C. K. N. Patel, R. E. Slusher and P. A. Fleury, Phys. Rev. Letters 17, 1011 (1966);  
J. J. Wynne, Technical Report No. 568, Division of Engineering and Applied Physics, Harvard University (August 1968).
46. H. Brooks, Advances in Electronics and Electron Physics, Vol. VII (Academic Press, New York, 1955), p. 129.
47. Sh. M. Kogan, Sov. Phys.—Solid State 4, 1813 (1963).
48. G. Ascarelli and S. Rodriguez, Phys. Rev. 124, 1321 (1961).
49. D. R. Hamann and A. L. McWhorter, Phys. Rev. 134, A250 (1964); M. Lax, Phys. Rev. 119, 1502 (1960).
50. P. A. Wolff and G. A. Pearson, Phys. Rev. Letters 17, 1015 (1966).
51. P. Kaw, Phys. Rev. Letters 21, 539 (1968); B. S. Krishnamurthy and V. V. Paranjape, Phys. Rev. 181, 1153 (1969); L. Stenflo, Phys. Rev. B 1, 2821 (1970).
52. R. J. Sladek, Phys. Rev. 120, 1589 (1960).

## IV. MICROELECTRONICS

### A. LOW TCR TANTALUM NITRIDE RESISTORS

A technique for sputtering tantalum nitride resistors of near zero temperature coefficient of resistance (TCR) is under development. Low TCR tantalum nitride resistors have recently been reported.<sup>‡</sup> However, these resistors are formed by DC sputtering tantalum in a partial pressure of nitrogen onto 7059 glass held at a temperature between 250° to 300°C. The resistors are subsequently heat treated in a vacuum at temperatures in excess of 500°C and stabilized at 300°C. The resistors reported here are formed by RF sputtering tantalum in a partial pressure of nitrogen onto 99.5% Al<sub>2</sub>O<sub>3</sub> substrates which have far better thermal properties than does glass.

TABLE IV-1 TCR OF TANTALUM NITRIDE RESISTORS AS A FUNCTION OF NITROGEN PARTIAL PRESSURE	
P <sub>N2</sub> (torrs)	TCR (ppm/°C) ± 10 Percent
1 × 10 <sup>-5</sup>	-105
5 × 10 <sup>-5</sup>	-120
1 × 10 <sup>-4</sup>	+2
5 × 10 <sup>-4</sup>	-1

No further treatment of the resistors is necessary except for a 2-hour stabilization anneal in air at 325°C. The substrates are not heated by an external source, but are electrically and thermally floated on a 0.048-inch thick piece of 7059 glass which allows the substrate to reach an equilibrium temperature dependent on RF power density.<sup>§</sup> TCR as a function of nitrogen partial pressure is shown in Table IV-1 for resistors sputtered at a total argon plus nitrogen pressure of 10 μ of mercury, a power density of 1.6 W/cm<sup>2</sup>, and a target to substrate distance of 5.7 cm. The resistors are stabilized at 325°C in air for 2 hours.

F. J. Bachner

### B. ALUMINUM INTERCONNECTIONS AND BEAM LEADS ON POLYIMIDE SUBSTRATES

Work is in progress to develop techniques and evaluate materials useful for forming aluminum interconnections and beam leads on polyimide substrates. The problems encountered are in two areas: first, etching the interconnect and beam lead pattern on the polyimide before the apertures are opened in the substrate; second, opening the apertures in the polyimide without destroying the overhanging aluminum beams.

<sup>‡</sup> A. Sato, Y. Oda and Y. Hishimura, Proceedings of Electronic Components Conference, Washington, D.C., May 1970, p. 58.

<sup>§</sup> J.S. Logan, S.S. Maddocks and P.D. Davidse, IBM J. Res. Develop. 14, 182 (1970).



## Section IV

Etching the aluminum interconnections and beams requires the proper selection of starting materials combined with suitable photolithographic techniques. The aluminum on the polyimide must be sufficiently thick to give beams of suitable strength (about 0.0005 inch minimum), but not so thick that undercutting during etching becomes a problem. The aluminum must also be of very high purity to give good line definition during etching, and must be attached to the polyimide in a manner that does not leave deleterious residues when the aluminum is etched away. Two types of material have been evaluated. Aluminum vacuum evaporated directly onto the polyimide has proven very easy to etch, but the deposits are highly strained causing the beams to curl up when the underlying polyimide is removed. However, the evaporated films were considerably less than 0.0005 inch thick, and thicker films may prove sufficiently stable despite the stresses in the deposit. The second type of material has the polyimide formed by polymerization directly onto high-purity aluminum foil. This type of material is not easily obtained, however, and the samples given us for evaluation had a 0.002-inch foil which presented severe etching problems. The photoresists normally used — KTFR, KMER and the AZ family — do not have sufficient adhesion to the aluminum to allow etching such thick foils. Nevertheless, some limited success has been achieved using Dynachem resists.

The problem in opening the apertures in the polyimide has been to find an etch that would attack the polyimide but not the aluminum, and then to find a suitable masking material to define the holes in the polyimide. The etch selected is a 1:9 by volume solution of  $H_2O$  and 95-percent hydrazine used at room temperature. Masking against the hydrazine with metals requires a lamination or evaporation process. The lamination process is undesirable because of the nature of the epoxies used; the evaporation technique is expensive, time consuming, and requires a selective etch that will attack the masking metal and not the aluminum. Unfortunately, none of the liquid photoresists will stand up to the hydrazine solution. However, Riston — a sheet photoresist product of the DuPont Company — has proven to be an excellent mask. The Riston is rolled onto the polyimide with both at approximately 80°C, is exposed as a negative-acting resist, and, after etching, can be left on or stripped off with trichloroethylene or a commercial photoresist stripper such as J-100.

F. J. Bachner  
R. A. Cohen

### C. COMPUTER-AIDED DESIGN (CAD) AND MASK FACILITY

The interactive version of CIRCUS has been completed and the documentation distributed. Demand for use of the program is expected in the coming months.

The mask-making facility has continued to turn out an increasing volume of masks for many groups throughout the Laboratory, while refining techniques in this field. Chrome masks have become the standard for photorepeat tasks. Production has temporarily stopped for darkroom enlargement and redesign and for removal of the mask-generating equipment to a cleaner and more environmentally stable room. The result of these changes should be higher mask yield and greater production volume.

N. B. Childs

DOCUMENT CONTROL DATA - R&D

(Security classification of title, body of abstract and indexing annotation must be entered when the overall report is classified)

1. ORIGINATING ACTIVITY (Corporate author) Lincoln Laboratory, M.I.T.		2a. REPORT SECURITY CLASSIFICATION Unclassified													
		2b. GROUP None													
3. REPORT TITLE Solid State Research															
4. DESCRIPTIVE NOTES (Type of report and inclusive dates) Quarterly Technical Summary - 1 May through 31 July 1970															
5. AUTHOR(S) (Last name, first name, initial) McWhorter, Alan L.															
6. REPORT DATE 15 August 1970		7a. TOTAL NO. OF PAGES 72	7b. NO. OF REFS 93												
8a. CONTRACT OR GRANT NO. AF 19 (628)-5167		9a. ORIGINATOR'S REPORT NUMBER(S) Solid State Research (1970:3)													
b. PROJECT NO. 649L		9b. OTHER REPORT NO(S) (Any other numbers that may be assigned this report) ESD-TR-70-234													
c.															
d.															
10. AVAILABILITY/LIMITATION NOTICES This document has been approved for public release and sale; its distribution is unlimited.															
11. SUPPLEMENTARY NOTES None		12. SPONSORING MILITARY ACTIVITY Air Force Systems Command, USAF													
13. ABSTRACT  <p>This report covers in detail the solid state research work of the Solid State Division at Lincoln Laboratory for the period 1 May through 31 July 1970. The topics covered are Solid State Device Research, Materials Research, Physics of Solids, and Microelectronics. The Microsound work is sponsored by ABMDA and is reported under that program.</p>															
14. KEY WORDS <table border="0"><tr><td>solid state devices</td><td>electronic band structure</td><td>Raman scattering</td></tr><tr><td>materials research</td><td>proton bombardment</td><td>magneto-optical research</td></tr><tr><td>crystal growth</td><td>laser scattering</td><td>microelectronics</td></tr><tr><td>magnetism</td><td>infrared</td><td></td></tr></table>				solid state devices	electronic band structure	Raman scattering	materials research	proton bombardment	magneto-optical research	crystal growth	laser scattering	microelectronics	magnetism	infrared	
solid state devices	electronic band structure	Raman scattering													
materials research	proton bombardment	magneto-optical research													
crystal growth	laser scattering	microelectronics													
magnetism	infrared														